Computational study of hypersonic rarefied gas flow over re-entry vehicles using the second-order Boltzmann-Curtiss constitutive model

T. Chourushi[1], S. Singh[2], V. Asokakumar Sreekala[1], R. S. Myong[1*]

[1] *School of Mechanical and Aerospace Engineering and ACTRC, Gyeongsang National University, Jinju, Gyeongnam 52828, South Korea (T. Chourushi tushar@gnu.ac.kr; V. A Asokakumar Sreekala vishnuasokan@gnu.ac.kr; R. S. Myong myong@gnu.ac.kr)*

[2] *School of Physical and Mathematical Sciences, Nanyang Technological University, 21 Nanyang Link 637371, Singapore (S. Singh satyvir.singh@ntu.edu.sg)*

Abstract: The aerothermodynamics of re-entry vehicles vary significantly upon re-entry, descent, and landing, because of the drastic changes in atmospheric density and velocity. In highly rarefied regimes, the conventional Navier-Stokes-Fourier equations may not provide an accurate prediction of aerothermodynamic loads acting on these vehicles. To tackle these challenges, an explicit mixed-type modal discontinuous Galerkin method was developed, based on the second-order Boltzmann-Curtiss constitutive model and the Maxwell slip and Smoluchowski jump conditions. A comprehensive analysis was conducted for different configurations of re-entry vehicles under various degrees of rarefaction. The computational results show that the rotational mode of energy transfer for diatomic gases substantially affects the lift-to-drag ratio and stability of re-entry vehicles. The total drag and heat transfer rate of the second-order constitutive model remained smaller than those of the first-order constitutive model in the rarefied regime, which makes the second-order results in better agreement with the direct simulation Monte Carlo.

Keywords: Hypersonic re-entry vehicles; rarefied gas flows; discontinuous Galerkin method; constitutive model; diatomic gases; slip and jump conditions.

1* Corresponding author (R. S. Myong): Tel: +82-55-772-1645. 501 Jinjudaero, Jinju, Gyeongnam 52828, South Korea. Email: myong@gnu.ac.kr.

1. Introduction

With the introduction of commercial space operations, rapid advances are occurring in space flight, space exploration, and the development of recyclable spacecraft re-entry vehicles. The growing interest in hypersonic re-entry flight has motivated several research groups around the world to investigate the physics of hypersonic gas flows. Compared to traditional flight vehicles, hypersonic flight vehicles have a much larger flight envelope and undergo drastic changes in aerothermodynamic forces as they descend through atmospheric layers. Accordingly, understanding near- and highly non-equilibrium gas flows around the vehicle is crucial to designing high-performance hypersonic re-entry vehicles, and for risk management of mission failure. To date, accurately predicting aerothermodynamic loads on hypersonic vehicles has been one of the most challenging tasks, due to the poor understanding of high-temperature non-equilibrium flow physics and limited ground test facilities (Tsai et al. 2009; Schwartzentruber and Boyd 2015; Schouler, Prévereaud, and Mieussens 2020). Numerical modeling and simulation have subsequently become effective tools for studying the flow characteristics in hypersonic regimes (Hash et al. 2007; Li and Zhang 2009; Peng et al. 2016; Liang et al. 2018; Chinnappan et al. 2017; Chae et al. 2020; Mankodi et al. 2020; de Góes Maciel 2015; Noori and Karimian 2008; Sawley and Wüthrich 1995).

Hypersonic vehicles encounter different flow regimes as they fly through the atmosphere. These flow regimes are characterized based on the degree of rarefaction, commonly referred to as the Knudsen number. Previous studies have shown that the classical Navier-Stokes-Fourier equations without proper velocity slip and temperature jump boundary conditions are incapable of handling rarefied flow regimes and may not properly predict aerothermodynamic data (Santos 2007; Lofthouse, Scalabrin, and Boyd 2008; Hollis and Borrelli 2012; Guo et al. 2019; Jiang et al. 2019). To resolve this issue, the gas kinetic models based on the Boltzmann kinetic equation are often considered. So far, several numerical methods have been developed to solve the Boltzmann kinetic equation. The direct simulation Monte Carlo (DSMC) method (Bird 1994), although a very powerful tool, becomes computationally inefficient for low Knudsen number flows. On the other hand, the gas kinetic method based on the deterministic approach requires additional computational resources to compute near-continuum gas regimes because of limitations in predicting the proper time step and cell size. Moreover, in the case of

hypersonic flows, the addition of velocity space discretization significantly affects the computational requirements.

Myong (Myong 1999, 2001; 2004a; 2004b, 2011, 2016) developed a distinct approach, the so-called second-order nonlinear constitutive relations (NCCR) for rarefied and microscale gases, which is a thermodynamically consistent hydrodynamic model for monatomic, diatomic and polyatomic gases. An important result in these studies is that the constitutive relations between stresses (and heat flux) and the strain rate (and temperature gradient) are generally nonlinear and coupled in states far from thermal equilibrium. The NCCR was systematically derived from the Boltzmann-Curtiss equation (Eu and Ohr 2001; Curtiss 1981) based on Eu's modified moment method (Eu 1980, 1992) and Myong's closing-last balanced closure (Myong 2014). Unlike the original Boltzmann kinetic equation, the Boltzmann-Curtiss kinetic equation additionally introduces the angular momentum and azimuth angle associated with the rotational mode of molecules to the kinetic formulation. The NCCR has also been studied by other researchers (Jiang, Zhao, Yuan, Chen and Myong 2019; Jiang, Zhao, Chen, and Agarwal 2019; Jiang, Zhao, Chen, and Agarwal 2019; Yuan, Zhao, Jiang, and Chen 2021) who have used the implicit finite volume method (FVM) as a basic numerical scheme.

The implementation of the second-order NCCR model is not trivial and is numerically challenging, particularly for a multi-dimensional problem. Among several numerical methods, the discontinuous Galerkin (DG) method was used in this study based on the following grounds. It was known that the conventional FVM based on Godunov type schemes suffers a noticeable degradation in low Mach number flows (Dellacherie 2010) and mixed (high and low Mach number) flows near the frontal part of blunt body or flat plate (Raj et al. 2017). On the other hand, the NCCR model is envisioned to solve all three—the high Mach, the high Knudsen, and both—of regimes, including the high Knudsen and low Mach number regime, in a unified framework, which demands a capability to treat two extreme cases, high and low Mach number flows. This is the main factor in the present study to employ the DG method, which demonstrated the ability to compute high and low Mach number flows with a single framework without resorting to the time-preconditioning techniques that are normally required for the FVM.

In the past, Evans et al. (Evans, Morgan, and Hassan 2011) incorporated the DG method to

provide a solution of the collisionless Boltzmann-BGK kinetic equations for rarefied gases. Myong in 2014 (Myong 2014) successfully applied the multi-dimensional DG scheme to the second-order constitutive model to study some challenging problems of nonequilibrium gas flows. In this mixed-type DG method, the implicit nature of the second-order constitutive model was treated by introducing an auxiliary variable.

Xiao and Myong (Xiao and Myong 2014) presented an explicit modal two-dimensional DG scheme for conservation laws on unstructured triangular meshes in conjunction with an implicit NCCR model for monatomic gas past a cylinder and microscale shock vortex interaction (SVI) flows. Later, Singh et al. (Singh, Karchani, and Myong 2018) extended the implicit NCCR model by including the rotational mode of the diatomic and polyatomic gas molecules derived from the Boltzmann-Curtiss kinetic equations for the SVI flows. Singh et al. (Singh, Battiato, and Myong 2021; Singh and Battiato 2021a) further studied the flow morphology of a shock accelerated cylindrical light bubble in diatomic and polyatomic gases. Omid and Myong (Ejtehadi and Myong 2020) investigated the under-expanding jet in a dusty gas environment, and jet impingement on dusty surfaces under rarefied conditions. Recently, Singh et al. (Singh, Karchani, Chourushi, Myong 2021) presented a three-dimensional mixed modal DG scheme for an implicit NCCR model on unstructured tetrahedral meshes for hypersonic rarefied and microscale gas flows.

In contrast to the globally coupled mass matrix of the continuous finite element method, the DG formulation can incorporate either modal or nodal discontinuous basis functions which generate a local elemental mass matrix of the finite element formulation (Bassi and Rebay 1997; Cockburn and Shu 1998; Giraldo and Warburton 2008; Iannelli 2011; Alekseenko et al. 2012; Li and Zhang 2017; You and Kim 2019). The DG method has several features over other numerical methods, including robustness with strong mathematical properties, arbitrary triangulation with hanging nodes, *p*- adaptivity by varying the polynomial degree, and is highly parallelizable (Bochev et al. 2001; Shu 2016; Su et al. 2019; Franchina et al. 2019; Evans et al. 2019). Nevertheless, there are some challenges in the DG method. In particular, it involves high computational cost, memory requirement, and programming complexity compared to the finite volume method (Le et al. 2014). Exploiting the DG method's potential for simulating hypersonic gas flows, many inviscid gas flows have been investigated in this regime. However,

only a limited number of studies on heat transfer loads and the stability of hypersonic flows in rarefied flow regimes have been computed (Barter and Darmofal 2010; Burgess and Mavriplis 2012; Brazell and Mavriplis 2013; Ching et al. 2019; Chourushi et al. 2020). In addition, the majority of these works have considered the monatomic gases or the rotational mode of diatomic and polyatomic gases only at the equilibrium level (through the specific heat ratio), neglecting the additional nonequilibrium effects associated with the excess normal stress and bulk viscosity terms present in diatomic and polyatomic gases (Singh 2018).

The purpose of this work is to numerically investigate aerothermodynamic loads on three-dimensional hypersonic re-entry vehicles using the second-order Boltzmann-Curtiss constitutive model with velocity slip and temperature jump conditions in the framework of the explicit mixed modal DG method. The present study is significantly different from previous studies on the second-order constitutive models in terms of numerical methods and research goals. The major difference is that instead of the FVM of previous studies, the DG method that can analyze high and low Mach number flows within a single framework was developed and extended to a three-dimensional code. Another difference is that while previous studies focused on accurately describing the flow field around the re-entry vehicles, the present study went further to analyze the aerothermodynamic coefficients such as the lift-to-drag ratio and pitching moment required for the stability analysis of the re-entry vehicles. Section 2 presents the governing equations and zeroth, first-order, and second-order constitutive relations for monatomic, diatomic and polyatomic gases. Section 3 details the explicit modal DG method and the implementation of velocity slip and temperature jump boundary conditions. Section 4 presents the verification and validation of the computational code and investigates the hypersonic flow over various re-entry vehicles. Finally, in Section 5, concluding remarks and discussion of issues of further development in this topic are given.

2. Mathematical model

2.1. Physical conservation laws for diatomic and polyatomic gases

When there is no external force field, the Boltzmann-Curtiss kinetic equation for diatomic and linear polyatomic molecules with a moment of inertia I_m and angular momentum j can be expressed as follows (Curtiss 1981),

$$\left(\frac{\partial}{\partial t}+\mathbf{v}\cdot\nabla+\frac{j}{I_m}\frac{\partial}{\partial\psi}\right)f\left(\mathbf{v},\mathbf{r},\mathbf{j},\psi,t\right)=R\left[f\right], \tag{1}$$

where $f,\mathbf{v},\mathbf{r},\psi,j$ and $R\left[f\right]$ represent the distribution function of the population of molecules, the particle velocity, the particle position, the azimuthal angle associated with the orientation of the molecules, the magnitude of the angular momentum vector **j**, and the collision integral, respectively. Once we ignore the angular momentum of the molecule related to the rotational mode from the equation (1), the original Boltzmann kinetic equation for a monatomic gas is recovered,

$$\left(\frac{\partial}{\partial t}+\mathbf{v}\cdot\nabla\right)f\left(\mathbf{v},\mathbf{r},t\right)=C\left[f\right], \tag{2}$$

where $C\left[f\right]$ represents the Boltzmann collision integral of the interaction between two particles. The macroscopic quantities, conserved variables $\left(\rho,\rho\mathbf{u},\rho E\right)$, and the non-conserved variables such as the shear stress tensor $\mathbf{\Pi}$, the excess normal stress Δ, and the heat flux $\mathbf{Q}$ can be defined using the following statistical relationships (Eu and Ohr 2001):

$$\phi^{(h)}=\left\langle h^{(k)}f\right\rangle, \tag{3}$$

where the angular bracket denotes the integration over the microscopic variables $\mathbf{v},\mathbf{j},\psi$ in the computational domain. The $h^{(k)}$ indicates the molecular expression of the *h*-th moments of the distribution function and $\phi^{(h)}$ denotes the equivalent macroscopic quantity. The leading elements of the sets of the conserved and non-conserved variables in statistical forms are defined as follows (Eu and Ohr 2001),

$$\begin{aligned}&\phi^{(1)}=\rho,\ \phi^{(2)}=\rho\mathbf{u},\ \phi^{(3)}=\rho E,\\&\phi^{(4)}=\mathbf{\Pi}=\left[\mathbf{P}\right]^{(2)},\ \phi^{(5)}=\Delta=\frac{1}{3}\mathrm{Trace}\,\mathbf{P}-p,\ \phi^{(6)}=\mathbf{Q},\end{aligned} \tag{4}$$

where **u** is the velocity vector and *E* is the total energy density. The corresponding molecular expressions to this set read as,

$$h^{(1)} = m,\ h^{(2)} = m\mathbf{v},\ h^{(3)} = \frac{1}{2}mC^2 + H_{rot},$$
$$h^{(4)} = \left[m\mathbf{CC}\right]^{(2)},\ h^{(5)} = \frac{1}{3}mC^2 - p/n,\ h^{(6)} = \left(\frac{1}{2}mC^2 + H_{rot} - m\hat{h}\right)\mathbf{C}, \tag{5}$$

where m is the molecular mass of gas, $\mathbf{C} = \mathbf{v} - \mathbf{u}$ is the peculiar velocity of the molecule, n is the number density per unit mass, $\hat{h}$ is the enthalpy density per unit mass, and $H_{rot} = j^2/2I_m$ is the rotational Hamiltonian of the particle.

The viscous stress $\mathbf{\Pi}$ and excess normal stress Δ are related to the total stress tensor $\mathbf{P}$ through the relation,

$$\mathbf{P} = \frac{1}{3}\mathrm{Tr}(\mathbf{A})\mathbf{I} + \left[\mathbf{A}\right]^{(2)} = \left(p + \Delta\right)\mathbf{I} + \mathbf{\Pi}, \tag{6}$$

where $\mathbf{I}$ is the unit second rank tensor. The symbol $\left[\mathbf{A}\right]^{(2)}$ denotes the traceless symmetric part of the second-rank tensor $\mathbf{A}$. And the pressure p and temperature T terms are related through the equation of state as $p = nk_BT = \rho RT$.

The conservation laws of mass, momentum, and total energy for diatomic and polyatomic gases can be derived directly from the Boltzmann-Curtiss kinetic equation by noting that the molecular expressions for conserved variables are collision invariants, that is, $\left\langle h^{(1,2,3)} R\left[f\right]\right\rangle = 0$. Subsequently differentiating the statistical definition of the conserved variables with time and combining them with the Boltzmann-Curtiss kinetic equation, the following conservation laws, all of which are an exact consequence of the Boltzmann-Curtiss kinetic equation, can be derived (Myong 2004b, Singh, Karchani, and Myong 2018),

$$\frac{\partial}{\partial t}\begin{bmatrix}\rho\\ \rho\mathbf{u}\\ \rho E\end{bmatrix} + \nabla\cdot\begin{bmatrix}\rho\mathbf{u}\\ \rho\mathbf{uu} + p\mathbf{I}\\ \left(\rho E + p\right)\mathbf{u}\end{bmatrix} + \nabla\cdot\begin{bmatrix}0\\ \mathbf{\Pi} + \Delta\mathbf{I}\\ \left(\mathbf{\Pi} + \Delta\mathbf{I}\right)\cdot\mathbf{u} + \mathbf{Q}\end{bmatrix} = 0. \tag{7}$$

After the following dimensionless variables and parameters are introduced,

$$
\begin{aligned}
&t^* = \frac{t}{\left(L/u_r\right)},\quad \boldsymbol{x}^* = \frac{\boldsymbol{x}}{L},\ \nabla^* = L\nabla,\ \rho^* = \frac{\rho}{\rho_r},\quad \boldsymbol{u}^* = \frac{\boldsymbol{u}}{u_r},\quad p^* = \frac{p}{p_r},\ T^* = \frac{T}{T_r},\\
&E^* = \frac{E}{u_r^2},\quad C_p^* = \frac{C_p}{C_{pr}},\quad \mu^* = \frac{\mu}{\mu_r},\ k^* = \frac{k}{k_r},\\
&\boldsymbol{\Pi}^* = \frac{\boldsymbol{\Pi}}{\left(\mu_r u_r/L\right)},\ \Delta^* = \frac{\Delta}{\left(\mu_{b_r} u_r/L\right)},\quad \mathbf{Q}^* = \frac{\mathbf{Q}}{\left(k_r \Delta T/L\right)},
\end{aligned}
\tag{8}
$$

the non-dimensional conservation laws for diatomic and polyatomic gases can be written as (Myong 2004b, Raj et al. 2017),

$$
\frac{\partial \mathbf{U}^*}{\partial t^*} + \nabla^* \cdot \mathbf{F}_{inv}^* \left(\mathbf{U}^*\right) + \nabla^* \cdot \mathbf{F}_{vis}^* \left(\mathbf{U}^*, \boldsymbol{\Pi}^*, \Delta^*, \mathbf{Q}^*\right) = 0\,. \tag{9}
$$

In Eq. (8), the subscript *r* denotes the reference state, *L* denotes the characteristic length, C_p denotes the heat capacity per mass at constant pressure, and μ, μ_b, k represent the Chapman–Enskog shear viscosity, bulk viscosity, and thermal conductivity, respectively. In Eq. (9), the conservative vector $\left(\mathbf{U}^*\right)$, inviscid flux vector $\left(\mathbf{F}_{inv}^*\right)$, and viscous flux vector $\left(\mathbf{F}_{vis}^*\right)$ are defined as,

$$
U^* = \begin{bmatrix} \rho^* \\ \rho^* \mathbf{u}^* \\ \rho^* E^* \end{bmatrix}, \mathbf{F}_{inv}^* = \begin{bmatrix} \rho^* \mathbf{u}^* \\ \rho^* \mathbf{u}^* \mathbf{u}^* + \dfrac{1}{\gamma M^2} p^* \mathbf{I} \\ \left(\rho^* E^* + \dfrac{1}{\gamma M^2} p^*\right) \mathbf{u}^* \end{bmatrix}, \mathbf{F}_{vis}^* = \frac{1}{\mathrm{Re}} \begin{bmatrix} 0 \\ \boldsymbol{\Pi}^* + f_b \Delta^* \mathbf{I} \\ \left(\boldsymbol{\Pi}^* + f_b \Delta^* \mathbf{I}\right) \cdot \mathbf{u}^* + \dfrac{1}{\mathrm{Ec\,Pr}} \mathbf{Q}^* \end{bmatrix}. \tag{10}
$$

Here the dimensionless parameters such as the Mach number (*M*), Reynolds number (Re), Eckert number (Ec), and Prandtl number (Pr) can be defined as,

$$
M \equiv \frac{u_r}{\sqrt{\gamma R T_r}},\ \mathrm{Re} \equiv \frac{\rho_r u_r L}{\mu_r},\ \mathrm{Ec} \equiv \frac{(\gamma - 1) M^2}{\Delta T / T_r},\ \mathrm{Pr} \equiv \frac{C_{p_r} \mu_r}{k_r},\ C_p = \frac{\gamma R}{\gamma - 1},\ f_b = \frac{\mu_{b_r}}{\mu_r}. \tag{11}
$$

The factor $f_b = \mu_{b_r} / \mu_r$ is the ratio of the bulk viscosity to the shear viscosity. Its value is experimentally determined using a sound wave adsorption measurement (Cramer 2012). The specific heat ratio γ is assumed to be 1.667 for argon gas and 1.4 for nitrogen gas. And the

value of the Prandtl number is calculated through Eucken's relation,

$$\mathrm{Pr} = \frac{4\gamma}{9\gamma - 5}. \tag{12}$$

2.2. Constitutive models

2.2.1. First-order (Navier-Fourier) constitutive model

The first-order constitutive model (also known as Navier-Fourier) can be derived by differentiating the statistical definition of the non-conserved variables with time and combining them with the Boltzmann–Curtiss kinetic equation. Using these formulations, the shear stress tensor, the excess normal stress, and heat flux vector can be obtained,

$$\mathbf{\Pi}_0 = -2\mu\left[\nabla\mathbf{u}\right]^{(2)}, \quad \Delta_0 = -\mu_b \nabla\cdot\mathbf{u}, \quad \mathbf{Q}_0 = -k\nabla T \ . \tag{13}$$

Here the subscript 0 refers to the first-order Navier–Fourier constitutive model. During this process, the first-order balanced closure was applied (Myong 2014). And the following Chapman-Enskog linear transport coefficients are employed,

$$\mu = T^{\,s}, \ \mu_b = f_b\mu, \ k = T^{\,s}, \ \text{where } s = \frac{1}{2} + \frac{1}{\nu - 1}. \tag{14}$$

In this expression, the terms ν and s denote the index of the inverse power laws of the gas molecules and the exponent of the inverse power laws for the gas-particle interaction potentials, respectively. The value of s is assumed to be 0.81 for argon and 0.78 for nitrogen (Chapman and Cowling 1990). Once the Stokes' hypothesis is applied, that is, $\mu_b = 0$, the first-order Navier-Fourier model (13) is reduced to the well-known Navier-Stokes-Fourier (NSF) constitutive equations.

2.2.2. Second-order Boltzmann-Curtiss constitutive model

Similarly, the second-order constitutive model can be derived by first differentiating the statistical definition of the non-conserved variables $h^{(4,5,6)}$ with time and then combining it with the Boltzmann-Curtiss kinetic equation (Myong 2001; Eu 1992). However, the derivation of the second-order constitutive model (also known as NCCR) is not straightforward and has

been a topic of interest in the past (Eu 1980; Grad 1949; Myong 1999) mainly because of two fundamental issues (Myong 1999): the so-called closure problem and accurate treatment of the dissipation terms.

Myong in 2014 proposed a new closure theory (Myong 2014), known as the "closing-last balanced closure," from a keen observation of the essence of the closure problem in a complex system. In this balanced closure theory, the number of places to be closed in moment equations must be two, that is, kinematic (movement) and dissipation (interaction). Moreover, to accurately calculate the dissipation terms while making the underlying theory compatible with the second law of thermodynamics, Eu in 1980 proposed a cumulant expansion based on the canonical distribution function in the exponential form for the explicit calculation of the dissipation term (Eu 1992, 1980).

Moreover, the temporal dependence in the equations can be neglected, given the very short relaxation times (10^{-10} seconds) of the non-conserved variables compared to those for the conserved variables and the characteristic times of the flow process (Eu 1992; Myong 1999). These so-called adiabatic approximations simplify the partial differential equation into a set of algebraic equations, which significantly reduces the numerical complexities involved in solving the constitutive equations. Once these tenets—the aforementioned closing-last balanced closure and Eu's cumulant—are applied and adiabatic approximations are introduced, the following second-order constitutive model for diatomic and polyatomic gases (Myong 2004b) can be derived,

$$\begin{aligned}
\hat{\mathbf{\Pi}} q_{2\mathrm{nd}}(c\hat{R}) &= \left[\hat{\mathbf{\Pi}}\cdot\nabla\hat{\mathbf{u}}\right]^{(2)} + \left(1+ f_b\hat{\Delta}\right)\hat{\mathbf{\Pi}}_0, \\
\hat{\Delta} q_{2\mathrm{nd}}(c\hat{R}) &= \frac{3}{2}\left(\hat{\mathbf{\Pi}} + f_b\hat{\Delta}\mathbf{I}\right):\nabla\hat{\mathbf{u}} + \hat{\Delta}_0, \\
\hat{\mathbf{Q}} q_{2\mathrm{nd}}(c\hat{R}) &= \hat{\mathbf{\Pi}}\cdot\hat{\mathbf{Q}}_0 + \left(1+ f_b\hat{\Delta}\right)\hat{\mathbf{Q}}_0,
\end{aligned} \tag{15}$$

where,

$$q_{2\mathrm{nd}}(c\hat{R}) = \frac{\sinh(c\hat{R})}{c\hat{R}}. \tag{16}$$

All terms in equations (15) are normalized using the following variables and parameters,

$$\hat{\boldsymbol{\Pi}} \equiv \frac{\boldsymbol{\Pi}}{p} = \frac{N_\delta}{p^*}\boldsymbol{\Pi}^*,\ \hat{\Delta} \equiv \frac{\Delta}{p} = \frac{N_\delta}{p^*}\Delta^*,\ \hat{\mathbf{Q}} \equiv \frac{\mathbf{Q}}{p\sqrt{\frac{C_p T}{2\,\mathrm{Pr}}}} = \frac{N_\delta}{p^*}\frac{\mathbf{Q}^*}{\sqrt{T^*/(2\varepsilon)}},$$
$$\nabla\hat{\mathbf{u}} \equiv \frac{-2\mu\nabla\mathbf{u}}{p} = -2\mu^*\frac{N_\delta}{p^*}\nabla^*\mathbf{u}^*,\ N_\delta \equiv \frac{\mu_r u_r / L}{p_r} = \frac{\gamma M^2}{\mathrm{Re}} = \mathrm{Kn}\, M\sqrt{\frac{2\gamma}{\pi}},\ \varepsilon \equiv \frac{1}{\mathrm{Ec}\,\mathrm{Pr}}\frac{1}{T_r/\Delta T}. \tag{17}$$

Here the caret (^) over a symbol represents a quantity with the dimension of the ratio of the stress $\boldsymbol{\Pi}$ to the pressure p and the ratio of the heat flux $\mathbf{Q}$ to a quantity $p(C_pT/2\,\mathrm{Pr})^{1/2}$. The values of $\boldsymbol{\Pi}_0$, Δ_0, and $\mathbf{Q}_0$ are determined by the linear Newtonian law of shear and bulk viscosity, and the linear Fourier law of heat conduction, respectively. The constant c, which is given by $c = \left[{}^{2\sqrt{\pi}}\!/_{5}\, A_2(\nu)\Gamma\left(4 - {}^{2}\!/_{\nu-1}\right)\right]^{1/2}$, has a value between 1.0138 (Maxwellian) and 1.2232 ($\nu = 3$); for instance, 1.018 for the nitrogen gas molecule (Myong 2004b). The tabulated values of $A_2(\nu)$ are taken from the literature (Chapman and Cowling 1990).

Some simplifications have been made when deriving the second-order constitutive relation of heat flux, the third equation in Eq. (15) (Myong 1999). Pure convective terms present in the constitutive equations were neglected because they are strictly zero in the one-dimensional velocity-shear flow and their contributions are not large compared to the other terms. Also, the $\mathbf{Q}\cdot\nabla\mathbf{u}$ term was omitted because it has the same property (heat flux times viscous stress) as the $\boldsymbol{\Pi}\cdot\nabla T$ term.

The Rayleigh-Onsager dissipation function $\hat{R}$ can be defined as,

$$\hat{R} = \left[\hat{\boldsymbol{\Pi}} : \hat{\boldsymbol{\Pi}} + 2\gamma' f_b \hat{\Delta}^2 + \hat{\mathbf{Q}}\cdot\hat{\mathbf{Q}}\right]^{1/2}. \tag{18}$$

The dissipation function "$\hat{R}$" is represented by the sum of the double scalar product between tensors and the dot product of the heat flux vector, which gives a direct measure of departure from equilibrium. The first-order cumulant approximation for the nonlinear factor "$q_{2\mathrm{nd}}(c\hat{R})$" (16) describes the mode of energy dissipation accompanying the irreversible processes and is directly related to the nonequilibrium entropy production in the system (Myong 2004b, Eu 1992).

The derivation of the hyperbolic sine function in Eq. (16) can be found in detail in references (Eu 1980; Eu 1981; Myong 2014). The concept of dissipation functions for irreversible processes was introduced by Lars Onsager in 1931 (Onsager 1931). The derivation of the constant c can be found in detail in reference (Myong 1999). Note that, when $q_{2\text{nd}}(c\hat{R})$ is assumed to be first-order, that is, $q_{1\text{st}} = 1$, all the coupled terms in the left-hand side of equations (15) are neglected, and the corresponding first-order constitutive model exactly recovers the Navier-Fourier model (13).

At this stage, it should be mentioned that the bulk viscosity μ_b can be viewed as a quantity directly related to the relaxation time associated with the rotational degrees of freedom. In addition, it can be shown that the excess normal stress Δ appearing in the conservation laws (10) and second-order Boltzmann-Curtiss constitutive model (15) is equivalent to the difference between the translational and rotational temperatures (McCourt, Beenakker, Köhler, and Kuščer 1990; p. 276). Therefore, the rotational mode of diatomic gas molecules was already embedded in the NCCR model through the excess normal stress Δ. Furthermore, the hydrodynamic equation can be formulated in two ways: either introducing the excess normal stress Δ and keeping one temperature concept or introducing two temperatures but no excess normal stress. The former was taken in the present study because it is a natural extension of the first-order Navier-Fourier constitutive model (13) and the one-temperature hydrodynamics is more natural to connect with the laws of thermodynamics.

Figure 1 shows the general features of the first- and second-order constitutive models for monatomic and diatomic gases in the compression-expansion flow. The second-order constitutive model shows the non-linear asymmetric relation of the normal stress for the case of rapid compression and expansion of gas. Although slight differences are observed in the profile of second-order constitutive models for monatomic and diatomic gases, the general pattern remains the same (Singh, Karchani, Sharma, and Myong 2020).

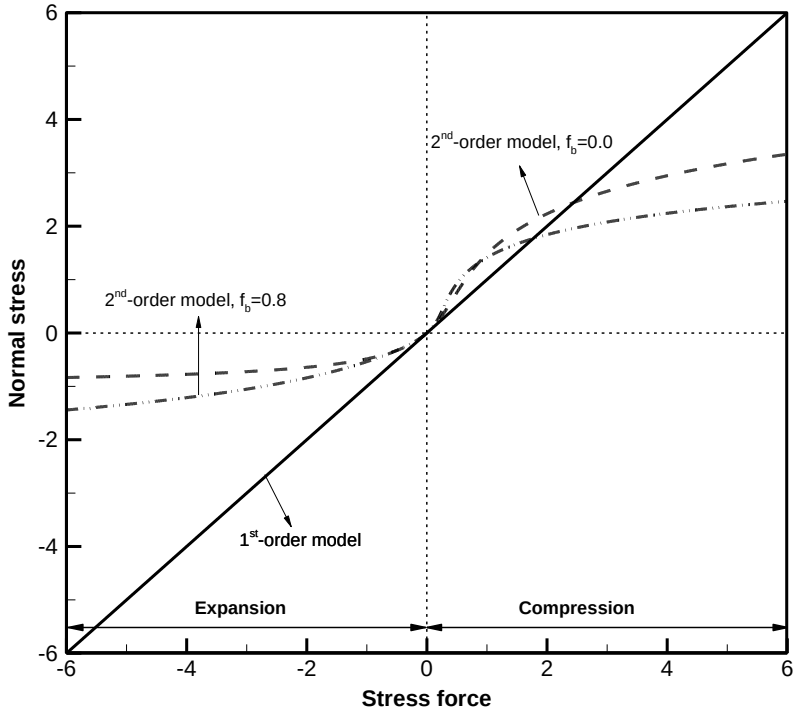

Fig. 1. First-order and second-order solutions of the Boltzmann–Curtiss-based constitutive model for monatomic ($f_b = 0.0$) and diatomic ($f_b = 0.8$) gases in a compression - expansion flow.

3. Mixed discontinuous Galerkin

3.1. Mixed-type modal discontinuous Galerkin scheme

In the present work, an in-house mixed modal discontinuous Galerkin (DG) formulation developed by Myong and co-authors (Raj et al. 2017; Le et al. 2014; Singh and Myong 2017; Singh and Battiato 2021; Chourushi et al. 2020; Chourushi et al. 2022) is employed. The mixed-type method plays a critical role in the present DG method because the standard DG method cannot handle the spatial discretization of the conservation laws (9) in conjunction with the highly non-linear and implicit form of the second-order constitutive relations (15). In this mixed DG formulation, an additional auxiliary variable " Θ " is introduced to handle the second-order derivatives appearing in the implicit constitutive relations of viscous stress and heat flux. This auxiliary variable Θ can be defined as the derivative of either primitive or conservative variables. To apply the mixed DG formulation, the conservation laws (9) (with

the asterisks omitted for notational brevity) can be expressed as a coupled system for $\mathbf{U}$ and Θ as,

$$\begin{aligned} &\Theta - \nabla \mathbf{U} = 0, \\ &\frac{\partial \mathbf{U}}{\partial t} + \nabla \cdot \mathbf{F}_{inv}\left(\mathbf{U}\right) + \nabla \cdot \mathbf{F}_{vis}\left(\mathbf{U}, \Theta\right) = 0. \end{aligned} \tag{19}$$

These coupled systems of equations are then solved over the computational domain by decomposing them into unstructured triangular or tetrahedral elements. Thereafter, the exact solutions for $\mathbf{U}$ and Θ are approximated using the DG polynomial approximations of $\mathbf{U}_h$ and Θ_h, respectively,

$$\begin{aligned} \mathbf{U}_h\left(\mathbf{x}, t\right) &= \sum_{i=0}^{N_k} \mathrm{U}_h^i(t) b_i(\mathbf{x}), \\ \Theta_h\left(\mathbf{x}, t\right) &= \sum_{i=0}^{N_k} \Theta_h^i(t) b_i(\mathbf{x}), \quad \mathbf{x} \in \Omega_e, \end{aligned} \tag{20}$$

where $\hat{\mathrm{U}}_h^i$, $\hat{\Theta}_h^i$ are the local degrees of freedom of $\mathbf{U}$ and Θ, $b_i\left(\mathbf{x}\right)$ is the basis function for the finite element space, and N_k is the number of required basis functions for the *k*- exact DG approximation. Furthermore, the mixed system of equations (19) is multiplied with the test function, which is considered the same as the basis function b_h, and then integrated by parts over an element Ω_e, resulting in the following weak formulation of the mixed system,

$$\begin{aligned} &\int_{\Omega_e} \Theta_h b_h dV + \int_{\Omega_e} \nabla b_h \cdot \mathbf{U}_h dV - \int_{\partial\Omega_e} b_h \mathbf{U}_h \cdot \mathbf{n} d\Gamma = 0, \\ &\frac{\partial}{\partial t} \int_{\Omega_e} \mathbf{U}_h b_h dV - \int_{\Omega_e} \nabla b_h \cdot \mathbf{F}_{inv} dV + \int_{\partial\Omega_e} b_h \mathbf{F}_{inv} \cdot \mathbf{n} d\Gamma - \int_{\Omega_e} \nabla b_h \cdot \mathbf{F}_{vis} dV + \int_{\partial\Omega_e} b_h \mathbf{F}_{vis} \cdot \mathbf{n} d\Gamma = 0, \end{aligned} \tag{21}$$

where $\mathbf{n}$ is the outward normal vector, *V*, and Γ are the volume and surface integral of the element, respectively.

3.1.1. Decomposition of the multi-dimensional second-order constitutive model

The multi-dimensional second-order constitutive model in the surface integral was treated based on the concept of decomposition (Myong 1999, 2004b). The three-dimensional flow problem can be split into three sub-problems in the *x*, *y*, *z* directions. The stress and heat flux

components $(\Pi_{xx}, \Pi_{xy}, \Pi_{xz}, \Delta, Q_x)$ on a surface in a three-dimensional control volume induced by thermodynamic driving forces such as velocity gradients $\left(u_x, v_x, w_x\right)$ and temperature gradients $\left(T_x\right)$ can be approximated as the sum of three decomposed solvers; first on $\left(u_x, 0, 0, T_x\right)$ describing the compression-expansion flow, second on $\left(0, v_x, 0, 0\right)$, and third on $\left(0, 0, w_x, 0\right)$ describing the velocity-shear flow.

In contrast to the finite volume formulation where only the surface integral is required, the DG formulation requires a volume integral. To decompose the multi-dimensional second-order constitutive relations in the volume integral, the viscous flux in Eq. (10) is divided into three terms (*x*, *y*, *z* components) (Singh, Karchani, Chourushi, and Myong 2021). In the *x*-direction, the *x*-component of the viscous flux can be decomposed into primary (P) and secondary (S) parts. The primary and secondary parts of the viscous flux can be further decomposed into seven sub-parts.

3.1.2. Basis functions

In this work, basis functions based on the orthogonal Jacobi polynomials are considered for the triangular and tetrahedral elements, respectively. The Jacobi polynomials for the transformation of a physical domain into a computational domain between the interval $[-1, 1]$ can be written as (Singh 2018),

$$P_n^{\alpha,\beta} = \frac{(-1)^n}{2^n n!}(1+\xi)^{\alpha}(1+\xi)^{-\beta}\frac{d^n}{d\xi^n}\left\{(1-\xi)^{\alpha+n}(1-\xi)^{\beta+n}\right\} \quad \text{for } (\alpha,\beta) > -1, \tag{22}$$

where ξ refers to the coordinate of computational space, α, β denotes the coordinates of the element, and n refers to the order of the polynomial. These polynomials further reduce to the following generalized form (also known as the Legendre polynomial) by setting $\alpha = \beta = 0$ in Eq. (22) (Singh 2018; Li 2006),

$$L_n(\xi) = P_n^{0,0}(\xi) = \frac{(-1)^n}{2^n n!}\frac{d^n}{d\xi^n}\left(1-\xi^2\right)^n. \tag{23}$$

The total number of basis functions for the *k*-th order accurate polynomial for two and three-

dimensions are reconstructed as under (Singh 2018),

$$N_k = \begin{cases} \dfrac{(k+1)(k+2)}{2}, & \text{if } \mathrm{D}=2, \\ \dfrac{(k+1)(k+2)(k+3)}{6}, & \text{if } \mathrm{D}=3, \end{cases} \tag{24}$$

where D is the dimension. Using these relationships the total number of basis functions with an accuracy up to the 5th order are summarized in Table 1**.**

Table 1 Total number of basis functions for the computational element with an accuracy up to 5th order (Singh 2018).

Polynomial order	Two-dimensional	Three-dimensional
0	1	1
1	3	4
2	6	10
3	10	20
4	15	35
5	21	56

In the 2D problem, Dubiner basis functions (Dubiner 1991) were used for the triangular elements, where a collapsed coordinate transformation was used to transfer triangles in the physical domain to the standard square elements. Another transformation was introduced to transfer the triangle in the physical space to the computational space where the new local coordinates have independent bounds $(-1 \le \xi \le 1,\ \xi + \eta = 0)$, and accuracy up to the 2nd order, and are summarized as (Ejtehadi and Myong 2020):

$$b_i(\xi,\eta) = \begin{cases} 1, \\ 2\xi + \eta + 1, \\ (3\eta + 1)/2, \\ 6\xi^2 + \eta^2 + 6\xi\eta + 6\xi + 4\eta + 1, \\ (5\eta^2 + 2\eta - 1)/2, \\ (5\eta^2 + 10\xi\eta + 6\xi + 8\eta + 3)/2. \end{cases} \tag{25}$$

Then the derivatives of the basis function are computed as,

$$\begin{aligned}\frac{\partial b_k}{\partial x} &= \frac{\partial b_k}{\partial \xi}\frac{\partial \xi}{\partial x} + \frac{\partial b_k}{\partial \eta}\frac{\partial \eta}{\partial x},\\ \frac{\partial b_k}{\partial y} &= \frac{\partial b_k}{\partial \xi}\frac{\partial \xi}{\partial y} + \frac{\partial b_k}{\partial \eta}\frac{\partial \eta}{\partial y}.\end{aligned} \tag{26}$$

On the other hand, in the 3D problem, scaled Legendre basis functions with an accuracy up to the 2nd order, the same as those in the references (Singh 2018; Singh and Myong 2019), were used for the tetrahedral elements as follows,

$$b_i(\xi,\eta,\zeta) = 10\begin{cases} 1, \\ -1+2\xi+\eta+\zeta, \\ -1+3\eta+\zeta, \\ -1+4\zeta, \\ (-1+2\xi+\eta+\zeta)(-1+5\eta+\zeta), \\ (-1+2\xi+\eta+\zeta)(-1+6\zeta), \\ (-1+3\eta+\zeta)(-1+6\zeta), \\ 2\xi^2+6\xi(-1+\eta+\zeta)+(-1+\eta+\zeta)^2, \\ 10\eta^2+8\eta(-1+\zeta)+(-1+\zeta)^2, \\ 1+5\zeta(-2+3\zeta). \end{cases} \tag{27}$$

Then the derivatives of the basis function are calculated as,

$$\begin{aligned}\frac{\partial b_k}{\partial x} &= \frac{\partial b_k}{\partial \xi}\frac{\partial \xi}{\partial x} + \frac{\partial b_k}{\partial \eta}\frac{\partial \eta}{\partial x} + \frac{\partial b_k}{\partial \zeta}\frac{\partial \zeta}{\partial x},\\ \frac{\partial b_k}{\partial y} &= \frac{\partial b_k}{\partial \xi}\frac{\partial \xi}{\partial y} + \frac{\partial b_k}{\partial \eta}\frac{\partial \eta}{\partial y} + \frac{\partial b_k}{\partial \zeta}\frac{\partial \zeta}{\partial y},\\ \frac{\partial b_k}{\partial z} &= \frac{\partial b_k}{\partial \xi}\frac{\partial \xi}{\partial z} + \frac{\partial b_k}{\partial \eta}\frac{\partial \eta}{\partial z} + \frac{\partial b_k}{\partial \zeta}\frac{\partial \zeta}{\partial z}.\end{aligned} \tag{28}$$

Furthermore, the number of Gaussian quadrature points increases with the order of accuracy of the DG approximations. In the present case k=1 (DG polynomial "p1") is being used (Chourushi et al. 2020; Singh 2018).

3.1.3. Numerical fluxes

In the DG weak formulation, both the boundary and surface integrals are approximated using the numerical quadrature rule (as illustrated in Table 2) with a few integration points consistent with the required accuracy (Singh 2018). This work considers local Lax-Friedrichs (LLF) and BR1 fluxes for the formulation of inviscid and viscid fluxes, respectively. Although the monotone LLF flux is the most dissipative, it is commonly used due to its computational efficiency and improved numerical stability. On the other hand, the BR1 flux is used to calculate the auxiliary and viscous fluxes at the elemental interfaces. These flux formulations for both inviscid and viscid fluxes can be written as,

$$\begin{aligned}
&\mathbf{F}_{inv}\cdot\mathbf{n}\approx\mathbf{H}_{inv}\left(\mathbf{U}_h^-,\mathbf{U}_h^+\right)=\frac{1}{2}\left[\mathbf{F}_{inv}\left(\mathbf{U}_h^-\right)+\mathbf{F}_{inv}\left(\mathbf{U}_h^+\right)-\alpha\left(\mathbf{U}_h^+-\mathbf{U}_h^-\right)\right],\\
&\mathbf{U}_h\cdot\mathbf{n}\approx\mathbf{H}_{aux}\left(\mathbf{U}_h^-,\mathbf{U}_h^+\right)=\frac{1}{2}\left[\mathbf{U}_h^-+\mathbf{U}_h^+\right],\\
&\mathbf{F}_{vis}\cdot\mathbf{n}\approx\mathbf{H}_{vis}\left(\mathbf{U}_h^-,\Theta_h^-,\mathbf{U}_h^+,\Theta_h^+\right)=\frac{1}{2}\left[\mathbf{F}_{vis}\left(\mathbf{U}_h^-,\Theta_h^-\right)+\mathbf{F}_{vis}\left(\mathbf{U}_h^+,\Theta_h^+\right)\right],\\
&\alpha=\max\left(\left|\mathbf{U}_h^-\right|+a_s^-,\left|\mathbf{U}_h^+\right|+a_s^+\right),
\end{aligned}\tag{29}$$

where $a_s=\sqrt{T}/M$ is the speed of sound at an elemental interface, and the superscripts $(+)$ and $(-)$ denote the left and right states of the element interface. Then, the substitution of Eq. (29) in Eq. (21) generates the weak formulation of the mixed form,

$$\begin{aligned}
&\int_{\Omega_e}\Theta_h b_h dV+\int_{\Omega_e}\nabla b_h\cdot\mathbf{U}_h dV-\int_{\partial\Omega_e}b_h\mathbf{H}_{aux}d\Gamma=0,\\
&\frac{\partial}{\partial t}\int_{\Omega_e}\mathbf{U}_h b_h dV-\int_{\Omega_e}\nabla b_h\cdot\mathbf{F}_{inv}dV+\int_{\partial\Omega_e}b_h\mathbf{H}_{inv}d\Gamma-\int_{\Omega_e}\nabla b_h\cdot\mathbf{F}_{vis}dV+\int_{\partial\Omega_e}b_h\mathbf{H}_{vis}d\Gamma=0.
\end{aligned}\tag{30}$$

Assembling all the elemental contributions yields a system of semi-discrete ordinary differential equations in time for each element,

$$\frac{\partial\mathbf{U}_h}{\partial t}=\mathbf{M}^{-1}\mathbf{R}\left(\mathbf{U}_h\right),\tag{31}$$

where $\mathbf{M}$ and $\mathbf{R}\left(\mathbf{U}_h\right)$ refer to the elemental orthogonal mass matrix and the residual vector of the system of equations, respectively. These explicit systems of equations (31) are then solved using the three-stage, third-order accurate, strong stability preserving Runge-Kutta method

(TVD-RK) proposed by Shu and Osher (Cockburn and Shu 1998),

$$\begin{aligned}
\mathbf{U}_h^{(1)} &= \mathbf{U}_h^n + \Delta t\, \mathbf{M}^{-1}\mathbf{R}\left(\mathbf{U}_h\right), \\
\mathbf{U}_h^{(2)} &= \frac{3}{4}\mathbf{U}_h^n + \frac{1}{4}\mathbf{U}_h^{(1)} + \frac{1}{4}\Delta t\, \mathbf{M}^{-1}\mathbf{R}\left(\mathbf{U}_h^{(1)}\right), \\
\mathbf{U}_h^{n+1} &= \frac{1}{3}\mathbf{U}_h^n + \frac{2}{3}\mathbf{U}_h^{(2)} + \frac{2}{3}\Delta t\, \mathbf{M}^{-1}\mathbf{R}\left(\mathbf{U}_h^{(2)}\right).
\end{aligned} \tag{32}$$

Here the term Δt refers to the local time step for each element and is determined using the following relation,

$$\Delta t = \frac{CFL}{\left(2k+1\right)} \frac{h}{\left|\lambda_{\text{inv}}^{\max}\right| + d\left|\lambda_{\text{vis}}^{\max}\right| \dfrac{2k+1}{h}}, \tag{33}$$

where *CFL*, *h*, and d are the Courant-Friedrichs-Lewy number, the radius of the circumscribed sphere in the tetrahedral element Ω_e, and the dimension of the element, respectively (Singh 2018; Singh and Battiato 2020, 2021b).

Table 2 Symmetric quadrature points and weights for three-dimensional elements up to 3rd order (Singh 2018).

Polynomial order	Number of points	Coordinates			Weights (ω)
		ξ	η	ζ	
Three- dimensional tetrahedron elements in $[0, 1]^3$ space					
1	1	0.25000	0.25000	0.25000	1.00000
2	4	0.5854101	0.1381967	0.1381967	0.25000
		0.1381967	0.5854101	0.1381967	0.25000
		0.1381967	0.1381967	0.5854101	0.25000
		0.1381967	0.1381967	0.1381967	0.25000
3	5	0.25000	0.25000	0.25000	-0.80000
		0.50000	0.16667	0.16667	0.45000
		0.16667	0.16667	0.16667	0.45000
		0.16667	0.16667	0.50000	0.45000
		0.16667	0.50000	0.16667	0.45000

3.1.4. Higher-order limiters

3.1.4.1. Positivity preserving limiter

High-order numerical schemes are subjected to spurious numerical oscillations in the solutions due to steep gradients arising from the compression of density leading to negative values for density and pressure variables over time. In this work, we incorporated a positivity-preserving limiter to ensure that the pressure and density fields were positive for each element (Karchani and Myong 2016). To limit the density field at every element, a small value $\omega = \min\left(10^{-13}, \bar{\rho}, \bar{p}\right)$ based on the mean of the density and pressure fields for the target cell is computed. Then the positivity for the density field is ensured by computing the minimum value of density over different quadrature points of the local elements as,

$$\theta_1 = \min\left(\frac{\bar{\rho}-\omega}{\bar{\rho}-\rho_{\min}}, 1\right), \tag{34}$$

where θ_1 is the limited coefficient. The high-order density components of the density variables are then modified,

$$\mathbf{U}_h\left(\mathbf{x},t\right) = \hat{\mathrm{U}}_h^0\left(t\right)b_0\left(\mathbf{x}\right) + \theta_1\sum_{i=1}^{N_k}\hat{\mathrm{U}}_h^i\left(t\right)b_i\left(\mathbf{x}\right). \tag{35}$$

Once the positivity is satisfied for the density field, the pressure field is preserved at each local element using the following formulation,

$$p\left[\left(1-t\right)\bar{\mathbf{W}} + t\,\bar{\mathbf{U}}\right] = \omega, \quad 0 \le t \le 1, \tag{36}$$

where $\bar{\mathbf{W}}$ and $\bar{\mathbf{U}}$ are the mean solution and limited density solution in conservative variables, respectively. Thereafter, the second limited coefficient θ_2 is calculated by selecting the minimum value of t among all the quadrature points, and the high order components of the conservative variables are modified as,

$$\mathbf{U}_h\left(\mathbf{x},t\right) = \hat{\mathrm{U}}_h^0\left(t\right)b_0\left(\mathbf{x}\right) + \theta_2\sum_{i=1}^{N_k}\hat{\mathrm{U}}_h^i\left(t\right)b_i\left(\mathbf{x}\right). \tag{37}$$

3.1.4.2. Barth Jespersen limiter

In addition to the positivity preserving limiter, a slope limiter to constrain the polynomial basis function within admissible limits is considered. The Barth Jespersen algorithm (slope limiter) is based on an unstructured grid for piecewise-linear data. In this algorithm, given the cell average $\bar{\mathbf{U}}_h = \mathbf{U}_c$ and the gradient $(\nabla \mathbf{U})_c$, the maximum slope for a constrained reconstruction form is determined as follows,

$$\mathbf{U}_h(\mathbf{x}) = \mathbf{U}_c + \alpha_e (\nabla \mathbf{U})_c \cdot (\mathbf{x} - \mathbf{x}_c), \qquad 0 \le \alpha_e \le 1, \ \mathbf{x} \in \Omega_e, \tag{38}$$

where α_e refers to the correction factor given by,

$$\alpha_e = \min \begin{cases} \min\left\{1, \dfrac{\mathbf{U}_e^{\max} - \mathbf{U}_c}{\mathbf{U}_i - \mathbf{U}_c}\right\}, & \text{if } \mathbf{U}_i - \mathbf{U}_c > 0, \\ 1, & \text{if } \mathbf{U}_i - \mathbf{U}_c = 0, \\ \min\left\{1, \dfrac{\mathbf{U}_e^{\min} - \mathbf{U}_c}{\mathbf{U}_i - \mathbf{U}_c}\right\}, & \text{if } \mathbf{U}_i - \mathbf{U}_c < 0. \end{cases} \tag{39}$$

Hence, the final solution values at several control points $\mathbf{x}_i \in \partial\Omega_e$ or in one of its neighbors Ω_a having a common boundary with Ω_e satisfy the following relation

$$\mathbf{U}_e^{\min} \le \mathbf{U}(\mathbf{x}_i) \le \mathbf{U}_e^{\max}, \quad \forall i. \tag{40}$$

Following the linearity, the solution $\mathbf{U}_h$ attains its extrema at the vertices $\mathbf{x}_i$ of the cell Ω_e.

3.2. Problem setup

A sketch of the computational domain and grid for the 2D Apollo vehicle is provided in Fig. 2. The far-field boundary condition was applied at a distance far enough from the vehicle. At the walls, slip and jump conditions were imposed. The temperature of the gas and walls were assumed to be 273 K. The hypersonic Mach number was considered to be 6. Both vibrational degrees of freedom for nitrogen gas and the chemical reactions of species were ignored. The Knudsen number was defined to measure the degree of rarefaction of gas (Tsien 1946; Myong 2014),

$$\mathrm{Kn} = \frac{\lambda}{L} = \frac{M}{\mathrm{Re}}\sqrt{\frac{\gamma\pi}{2}}, \tag{41}$$

where L is the characteristic length, which is taken as twice the maximum body radius $2R$ of the re-entry vehicle, M is the Mach number and Re is the Reynolds number. The mean-free-path λ is expressed as,

$$\lambda = \frac{k_B T}{\sqrt{2}\pi d^2 p}, \tag{42}$$

where k_B is Boltzmann's constant and d is the diameter of the gas molecule. The grid characteristics of a total of 23,923 unstructured triangular elements were used, with finer refinement in regions where flows were expected to evolve more severely. Similar grid characteristics were considered for the 2D OREX vehicle.

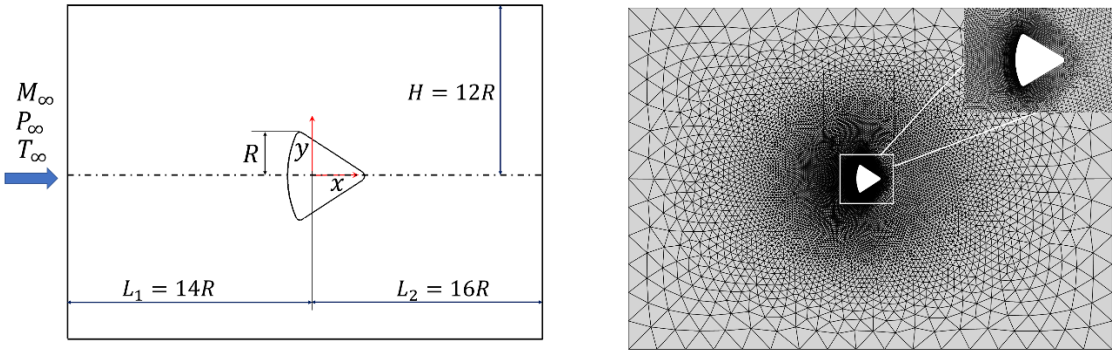

Fig. 2. Computational domain and grids characteristics for two- dimensional hypersonic flow over the Apollo vehicle.

The axisymmetric design of the 3D Apollo vehicle is sketched in Fig. 3, where the spherical blunt radius R_b, nose radius R_n, and shoulder radius R_s, are 1.9558 m, 4.6939 m, and 0.1956 m, respectively. The back shell has an inclination angle $\alpha_b = 33^0$, relative to the vehicle's axis of symmetry and the overall length of the vehicle is 3.4306 m. The quantities of interest for aerodynamic coefficients such as lift C_L, drag C_D , and pitching moment $C_{M,0}$ are outlined in Fig. 3 (b). The offset center of gravity (cg) was neglected as the focus of this work was to investigate the effects of flow parameters on the aerothermodynamic data of the re-entry vehicle.

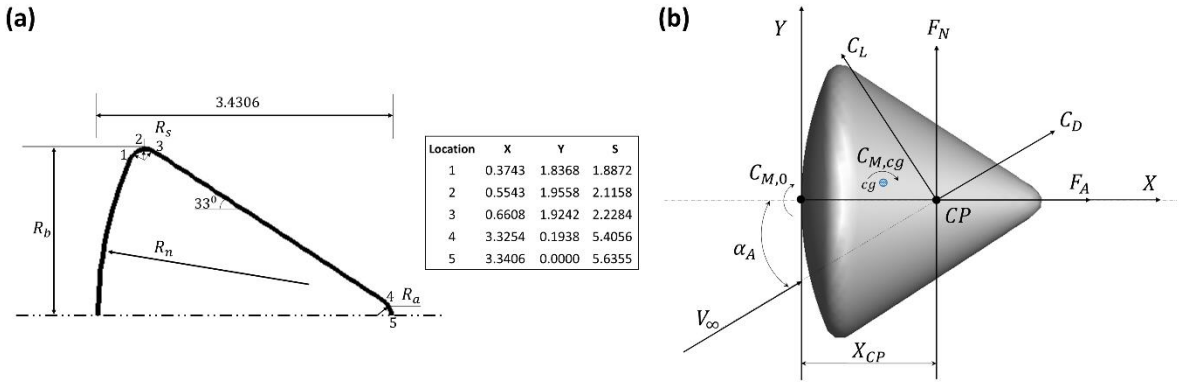

Location	X	Y	S
1	0.3743	1.8368	1.8872
2	0.5543	1.9558	2.1158
3	0.6608	1.9242	2.2284
4	3.3254	0.1938	5.4056
5	3.3406	0.0000	5.6355

Fig. 3. Sketch of the 3D Apollo vehicle: (a) outer mold line, and (b) definition of aerodynamic forces and moments.

Figure 4 shows the plot of aerodynamic data for nitrogen gas flow over a blunt reentry configuration with varied Mach and Knudsen numbers obtained by Schlegat (Schlegat 2016) using the experimental method. Influences from disturbances generated downstream were avoided by using a long wind tunnel. The pressure ratios were maintained between 10^{-5} to 10^{-8} for the reservoir and test section, and static pressure of less than 10^{-3} mbar was retained for the wind tunnel to minimize pressure disturbances. The reservoir temperatures were kept between 400 K to 1400 K, where the vibrational mode for nitrogen gas is partially excited. The Knudsen number was varied by varying the Mach number at a constant Reynolds number. Aerodynamic data such as lift, drag, and pitching moments were obtained at different Mach and Knudsen numbers.

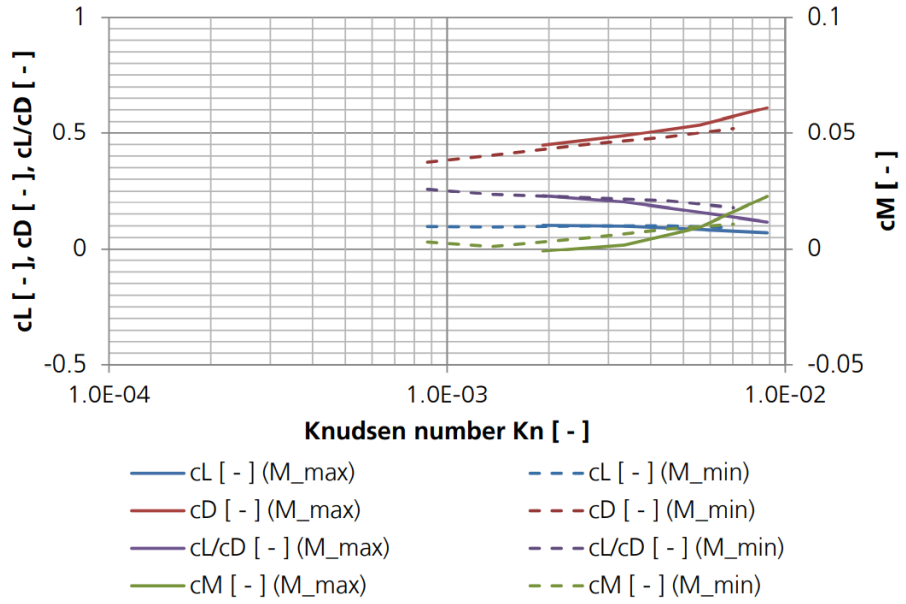

Fig. 4. Rarefaction effect on aerodynamic data obtained for nitrogen gas flow over a blunt re-entry vehicle at a flow angle of attack of 10^0, $M = 10$ (M_min) and $M = 25$ (M_max). (Taken from Schlegat's Ph.D. thesis (Schlegat 2016)).

3.3. Boundary conditions (slip and jump conditions) and their implementation

In the non-continuum regimes, gases close to solid surfaces are subjected to velocity slip and temperature jump conditions (Zhang, Meng, and Wei 2012). Among the various slip and jump models, the Langmuir slip and jump, Maxwell velocity slip, and Smoluchowski temperature jump conditions were considered in this study.

3.3.1. Langmuir slip and jump conditions

The gas-surface molecular interactions under Langmuir slip and jump conditions are calculated using the physical adsorption isotherm (Myong 2004a, 2016). In this method, the amount of gas molecules (adsorbate) on the absorbent is proportional to the pressure at a constant temperature. Then the gas-surface interaction process is expressed with the fraction α $(0 \le \alpha \le 1)$ of surface covered at equilibrium in dimensional form (Myong 2004a):

$$\alpha = \begin{cases} \dfrac{\beta_{\text{slip}} p}{1+\beta_{\text{slip}} p}, & \text{for monatomic gas,} \\ \dfrac{\sqrt[n]{\beta_{\text{slip}} p}}{1+\sqrt[n]{\beta_{\text{slip}} p}}, & \text{for diatomic } (n=2) \text{ and polyatomic } (n \geq 2) \text{ gas,} \end{cases} \tag{43}$$

where the equilibrium constant β_{slip} is given by

$$\beta_{\text{slip}} = \sqrt{\frac{\pi}{32}} \frac{\pi}{c^2} \frac{T_{ref}}{T_w} \exp\left(\frac{D_e}{k_B T_w} \right) \frac{1}{p_{ref} \text{Kn}}, \tag{44}$$

where c, p_{ref}, T_{ref}, Kn, and D_e are the gas constant of the exponent of the inverse power law of the particle interaction, the reference pressure, reference temperature, Knudsen number, and heat of adsorption, respectively. The velocity slip and temperature jump boundary conditions are then determined with the information about the fraction, α, and are written in a dimensional form as,

$$\begin{aligned} \mathbf{u} &= \alpha \mathbf{u}_{\text{wall}} + (1-\alpha)\mathbf{u}_{\text{gas}}, \\ T &= \alpha T_{\text{wall}} + (1-\alpha) T_{\text{gas}}, \end{aligned} \tag{45}$$

where $\mathbf{u}_{\text{wall}}$ is the velocity vector of the solid surface, T_{wall} is the temperature of the solid surface, and $\mathbf{u}_{\text{gas}}, T_{\text{gas}}$ are the gas velocity vector and temperature at the reference location, respectively.

3.3.2. Maxwell slip condition

The gas-surface molecular interactions in the Maxwell slip condition are evaluated based on the diffuse reflection of gas molecules from the solid surface; and consequently, the gas molecules are either considered approaching or receding streams (Kennard 1938). Moreover, an additional free parameter $\sigma_u \, (0 \leq \sigma_u \leq 1)$ is introduced to retain the conservation of momentum for the solid surface. Using this information, the Maxwell slip condition for the tangential velocity near a solid surface is related to the tangential shear stress $(\boldsymbol{\Pi}_{\tan})$ and the tangential heat flux $(\mathbf{Q}_{\tan})$ at the wall; in dimensional form as (Myong 2016; Chourushi et al. 2021),

$$\mathbf{u}_{\text{slip}} - \mathbf{u}_{\text{wall}} = -\left(\frac{2-\sigma_v}{\sigma_v}\right)\frac{\lambda_{\text{mean}}}{\mu}\boldsymbol{\Pi}_{\tan} - \frac{3}{4}\frac{\Pr(\gamma-1)}{\gamma p}\mathbf{Q}_{\tan}, \tag{46}$$

where $\mathbf{u}_{\text{wall}}$ refers to the velocity vector of a solid surface, and λ_{mean} denotes the mean free path. Also, the terms $\boldsymbol{\Pi}_{\tan}$ and $\mathbf{Q}_{\tan}$ can be defined in general coordinates as,

$$\begin{aligned}\boldsymbol{\Pi}_{\tan} &= (\mathbf{n}\cdot\boldsymbol{\Pi})\cdot\mathbf{S},\\ \mathbf{Q}_{\tan} &= \mathbf{Q}\cdot\mathbf{S},\end{aligned} \tag{47}$$

where the surface vector $\mathbf{S}$ is defined as $\mathbf{S} = \mathbf{I} - \mathbf{n}\otimes\mathbf{n}$ using the dyadic product ($\otimes$), which removes the normal components. Once the constitutive relations of viscous stress and heat flux are taken as linear with the first-order accuracy, the linear Maxwell slip condition in cartesian coordinates is recovered (Myong 2016; Myong et al. 2005; Singh 2018)

$$u_{\text{slip}} - u_{\text{wall}} = \left(\frac{2-\sigma_v}{\sigma_v}\right)\lambda_{\text{mean}}\frac{\partial u}{\partial y} + \frac{3}{4}\frac{\Pr(\gamma-1)}{\gamma p}k\frac{\partial T}{\partial x}. \tag{48}$$

3.3.3. Smoluchowski jump condition

By analogy with the Maxwell velocity slip condition, the Smoluchowski temperature jump boundary condition (Smoluchowski 1898) can be written as,

$$T_{\text{slip}} - T_{\text{wall}} = -\left(\frac{2-\sigma_T}{\sigma_T}\right)\frac{\lambda_{\text{mean}}}{k}\frac{2\gamma}{(\gamma+1)\Pr}\mathrm{Q}_{\text{normal}}, \tag{49}$$

where σ_T $(0 \le \sigma_T \le 1)$ denotes the thermal accommodation coefficient and $\mathrm{Q}_{\text{normal}}$ refers to the normal heat flux. Furthermore, once the constitutive relations of heat flux are taken as linear with the first-order accuracy, the simplified form of the temperature jump condition in cartesian coordinates is recovered,

$$T_{\text{slip}} - T_{\text{wall}} = \left(\frac{2-\sigma_T}{\sigma_T}\right)\lambda_{\text{mean}}\frac{2\gamma}{(\gamma+1)\Pr}\frac{\partial T}{\partial y}. \tag{50}$$

In the present study, both momentum (σ_u) and thermal accommodation (σ_T) coefficients were assumed to be unity.

4. Results and discussions

4.1. Validation of the DG code: High Mach number flow

The in-house modal discontinuous Galerkin method code has been extensively verified and validated in various problems of pure and dusty gas models under near- and non-equilibrium flow regimes (Xiao and Myong 2014; Le, Xiao, and Myong 2014; Singh, Karchani, and Myong 2018; Singh and Myong 2019; Ejtehadi et al. 2018, 2020; Chourushi et al. 2018, 2020). In this section, we performed a validation study specific to high Mach number flows.

In the validation test, we consider a two-dimensional hypersonic flow past a circular cylinder at Mach number (M=12) and Knudsen number (Kn=0.0118) for nitrogen gas. The temperature and density of the ambient gas are assumed to be $T_\infty = 217.45$ K, and $\rho_\infty = 7.48\times10^{-5}$ kg/m^3, respectively. An isothermal boundary condition with temperature $T_{\text{wall}} = 1000$ K was imposed on the cylinder surface. The geometric considerations of the 2D cylinder were taken to be the same as those of the reference (Schwartzentruber and Boyd 2008). Moreover, since the second-order constitutive model without the vibrational mode is used, we considered a direct comparison with a previous DSMC study (Schwartzentruber and Boyd 2008) in which energy transfer to vibrational modes is neglected.

Figure 5 illustrates the normalized temperature contour and heat flux coefficient for the first- and second-order constitutive models, and the existing DSMC solutions. It can be noted from the temperature contour plot that the bow shock structure of the second constitutive model is thicker than that of the first-order constitutive model due to the nonlinear characteristics associated with it. On the other hand, the plot for surface heat flux suggests that results of the second-order model are in closer agreement with the DSMC solutions than those of the first-order model.

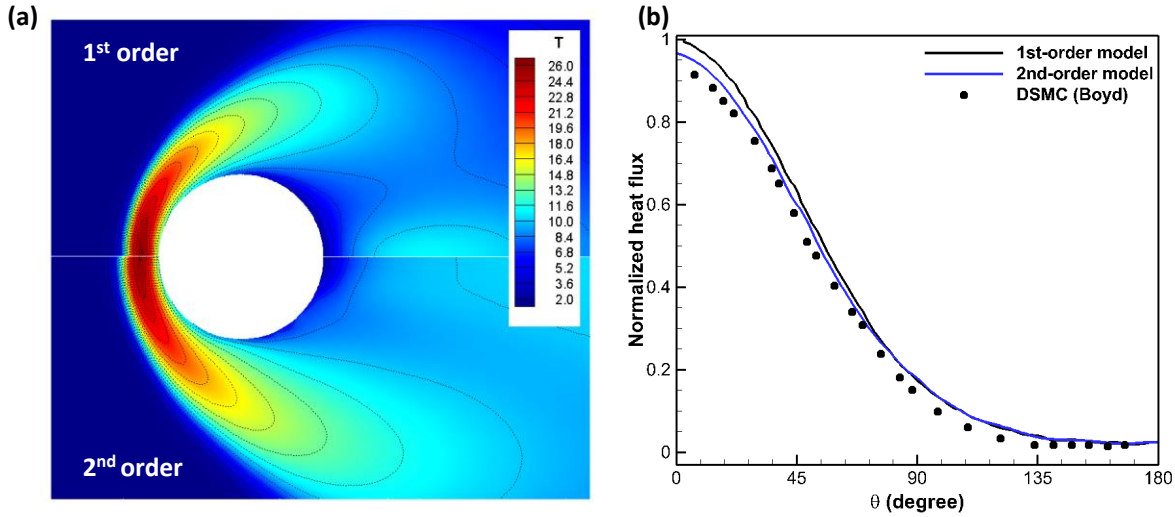

Fig. 5. Comparison of normalized flow properties in two-dimensional hypersonic flow past a circular cylinder problem obtained with the first- and second-order constitutive models and DSMC result (Schwartzentruber and Boyd 2008), for nitrogen gas, at $M = 12$ and $\mathrm{Kn} = 0.0118$: (a) temperature contour; and (b) heat flux coefficient.

4.2. Simulation of 2D OREX and Apollo vehicles: Rarefaction effects on aerothermodynamic data

Hypersonic (Mach number 6) flows of monatomic and diatomic gas over the Japanese Orbital Re-entry Experiment (OREX) and Apollo vehicles were also considered. The geometric details of the OREX and Apollo models are the same as those of the Yoshinaga et al. (Yoshinaga et al. 1996) and Schouler et al. (Schouler, Prévereaud, and Mieussens 2020), respectively. Like any other re-entry vehicle, these symmetric blunt-body configurations generate strong shock waves and dissipate the energy to reduce the surface heat flux. The quantities of interest are the aerothermodynamic coefficients of drag and heat flux. In all simulations, the flow angle of attack was assumed to be zero and aerodynamic moments associated with the non-zero angles of attack are delayed to the subsequent section of a three-dimensional re-entry vehicle.

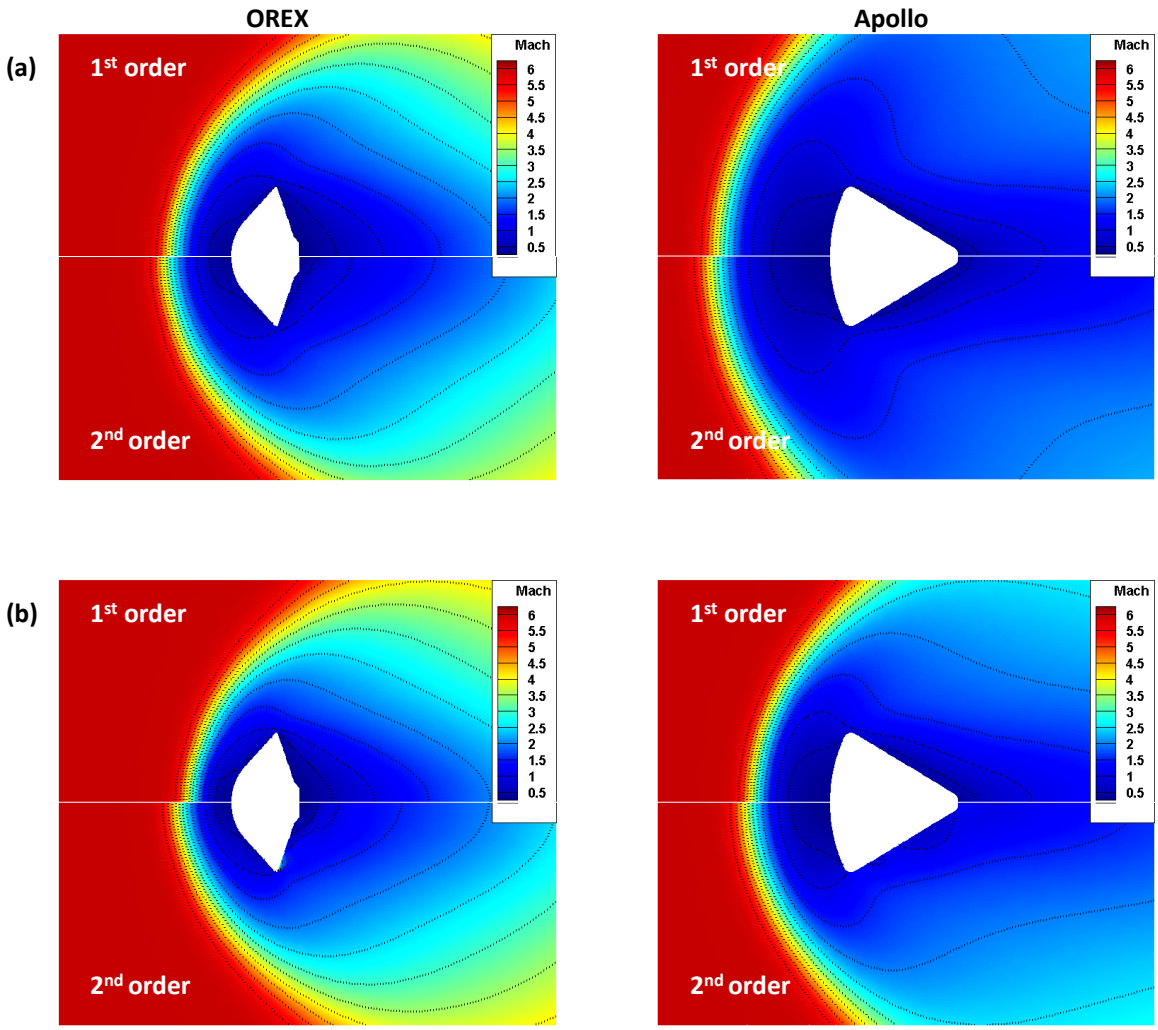

Fig. 6. Mach contours for hypersonic rarefied gas flow over the OREX (left side) and Apollo (right side) re-entry vehicles obtained with the first- and second-order constitutive models at $\alpha_A = 0^0$, $M = 6$ and $\mathrm{Kn} = 0.05$: (a) argon gas; (b) nitrogen gas.

Figure 6 compares the Mach contours for the hypersonic rarefied flow of argon and nitrogen gases over OREX and Apollo re-entry vehicles obtained using the first- and second-order constitutive models at zero degrees angle of attack and Knudsen number 0.05. It was observed that the stand-off shock moves further upstream for the argon gas when compared with the nitrogen gas. This is consistent with the well-known relationship that the shock stand-off distance for non-reactive gases is proportional to the ratio of the freestream density to the density immediately behind the shock (Belouaggadia et al. 2008), and that the ratio is greater

for monoatomic gases than for diatomic gases. Roughly, the order of difference for the shock stand-off distance for the Apollo vehicle is comparatively higher because of the increased bluntness of the frontal part of the body. Furthermore, the nonlinear property associated with the second-order model predicts a thicker shock front than the first-order model, resulting in a weaker compression inside the shock wave. In addition, the degree of a gaseous expansion predicted by the first-order model near the rear part of the vehicle is considerably higher than that of the second-order model.

Figure 7 compares the normalized temperature contours for the hypersonic rarefied flow of argon and nitrogen gases over the different re-entry vehicles. A stagnation region is formed between the bow shock and the blunt surface of the vehicle. The order of increase for the stagnation temperature of argon gas is substantially higher than that of the nitrogen gas. The variation in temperature for monatomic, diatomic, and linear polyatomic gases can be related to the specific heat capacity of gas, which is a function of specific heat ratio, as expressed by $C_P = \gamma R/(\gamma - 1)$. The specific heat capacity reduces with increasing specific heat ratio and consequently the gas cannot store a significant amount of kinetic energy and progressively transfers in the form of heat, which increases the overall temperature (Hwang 1971). Hence, an increase in stagnation temperature was noted for the monatomic gas when compared with the diatomic gas. Recently, Le et al. (Le et al. 2020) also reported an increase in stagnation temperature for argon gas compared with nitrogen gas for the hypersonic flow over a cylinder using both OpenFOAM (rhoCentralFoam) and DSMC simulations at varied Knudsen numbers (0.01 and 0.05). Further, a comparison of the overall temperature over re-entry vehicles suggests that the rise in stagnation temperature is relatively higher for the OREX vehicle.

A separated flow was observed near the backside region of the OREX vehicle due to the shape of the forebody, corner at the shoulder, and the back shell inclination angle of the vehicle. Owing to the presence of a re-circulating flow region immediately downstream of the OREX vehicle, a temperature rise is noted near the downstream region, as shown in Fig. 7 (a).

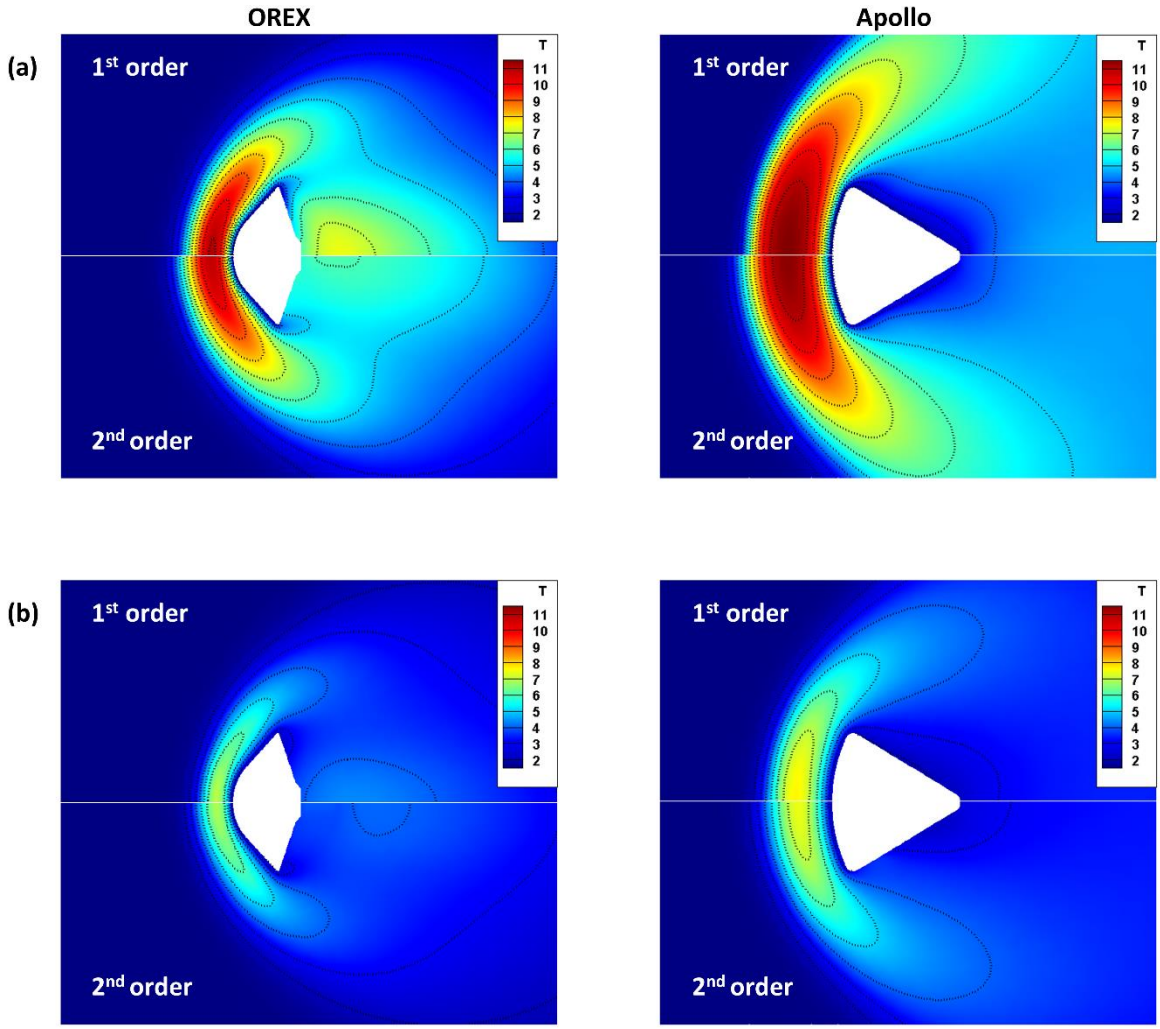

Fig. 7. Normalized temperature contours for hypersonic rarefied gas flow over the OREX (left side) and Apollo (right side) re-entry vehicles obtained with the first- and second-order constitutive models at $\alpha_A = 0^0$, $M = 6$ and $\mathrm{Kn} = 0.05$: (a) argon gas; (b) nitrogen gas.

Figure 8 compares the normalized surface variables for the hypersonic rarefied flow of argon gas over the OREX and Apollo vehicles with varied rarefaction parameters N_δ. As the rarefaction parameter increases, there is a significant increase in the order of normalized shear stress and heat flux, which is caused by the reduced freestream dynamic pressure and freestream power, respectively. In general, the aerothermodynamic heating over the OREX vehicle is significantly enhanced with increasing rarefaction compared with that of the Apollo vehicle, because of the relatively higher stagnation temperature. A closer examination of the

constitutive models suggests that the shear-thinning characteristics of the second-order model predict lower wall shear stress and heat flux when compared with the first-order model.

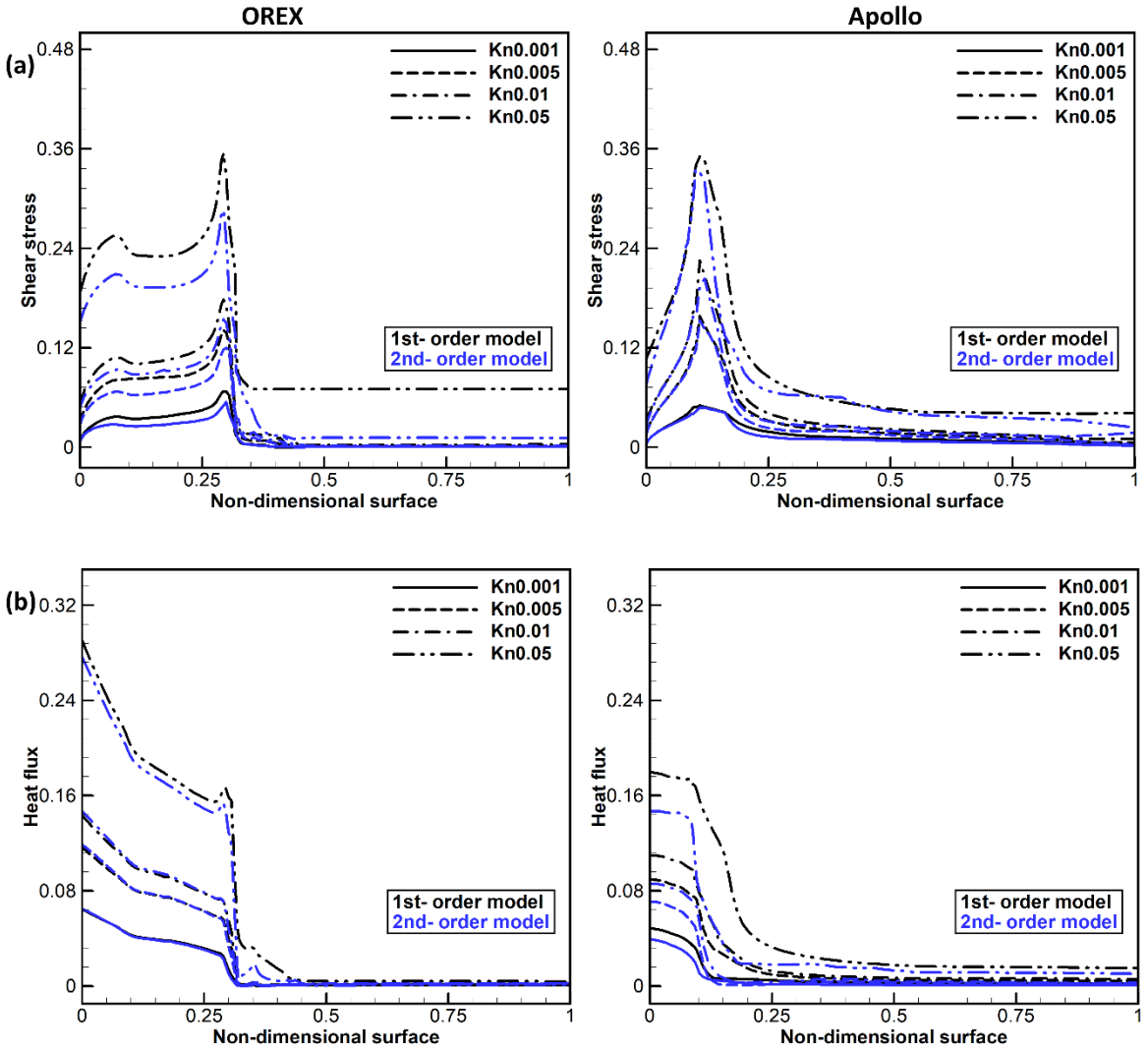

Fig. 8. Comparison of normalized surface variables for hypersonic rarefied argon gas measured on the surface of the OREX (left side) and Apollo (right side) re-entry vehicles with varied rarefaction parameters (N_δ) at $\alpha_A = 0^0$ and $M = 6$: (a) shear stress $\Pi_W / \left(\rho u_r^2 \right)$; (b) heat flux $Q_W / \left(\rho u_r^3 \right)$.

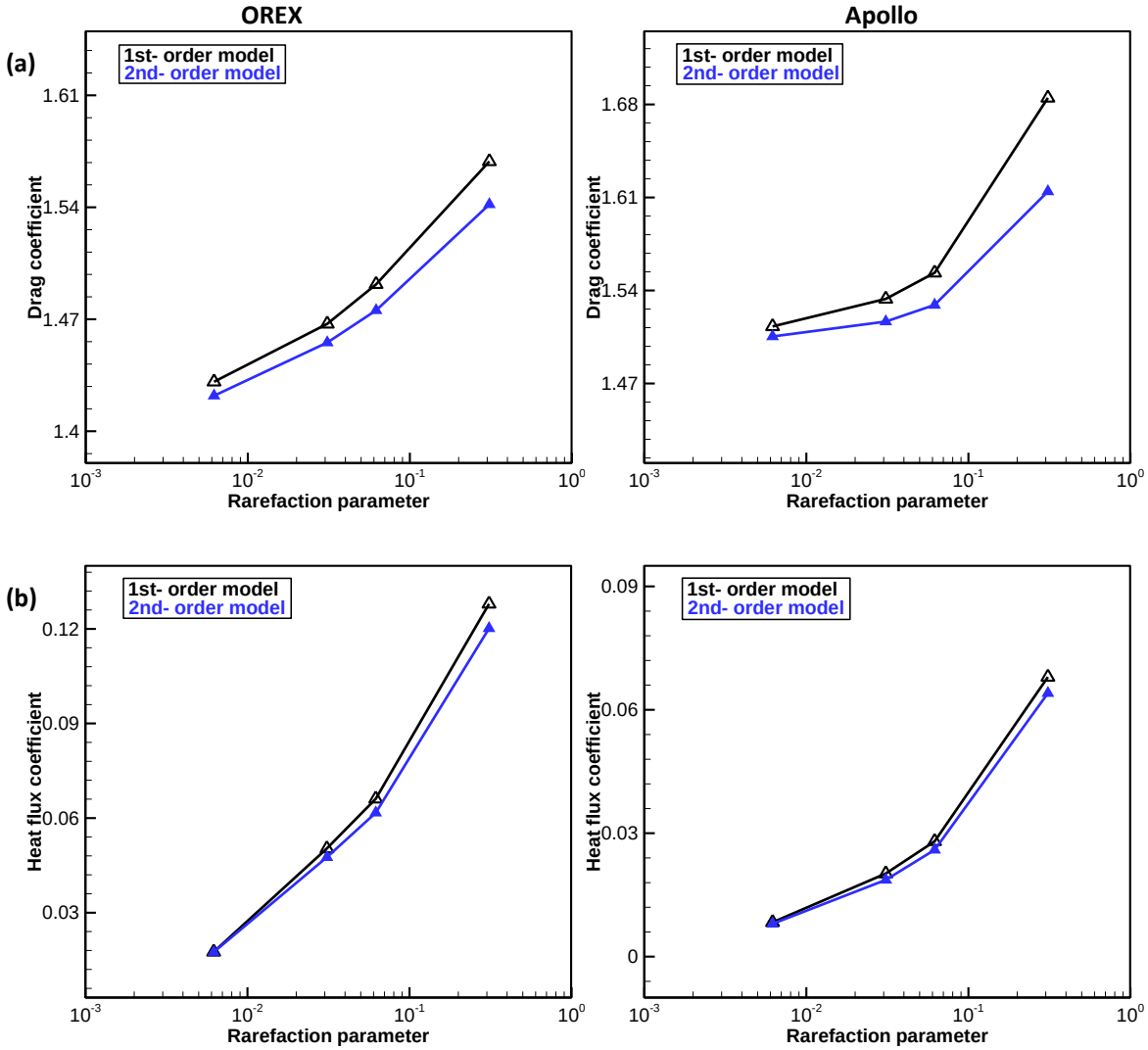

Fig. 9. Rarefaction effects on the aerothermodynamic data for the hypersonic rarefied flow of argon gas over the OREX (left side) and Apollo (right side) re-entry vehicles for varying degrees of rarefaction (N_δ) at $\alpha_A = 0^0$ and $M = 6$: (a) drag coefficient; (b) heat flux coefficient.

A further comparison of drag and heat flux coefficients for varying degrees of rarefaction is presented in Fig. 9. As the gas becomes more rarefied, fewer gas molecules interact with the surface, resulting in a reduction in drag. However, since the freestream dynamic pressure decreases more rapidly than the drag, the resultant drag coefficient (defined as drag divided by freestream dynamic pressure) increases. Similarly, an enhanced heat flux coefficient is observed because of the reduced freestream kinetic energy. It is seen that the drag coefficient for the OREX vehicle is lower than that of the Apollo vehicle due to the reduced resistance

from the smoother shape. Nonetheless, the heat flux coefficient for the OREX vehicle is relatively higher when compared with the Apollo vehicle. Besides, the second-order model predicts lower values for the drag and heat flux coefficients than the first-order model because of the shear-thinning characteristics for velocity and temperature, respectively.

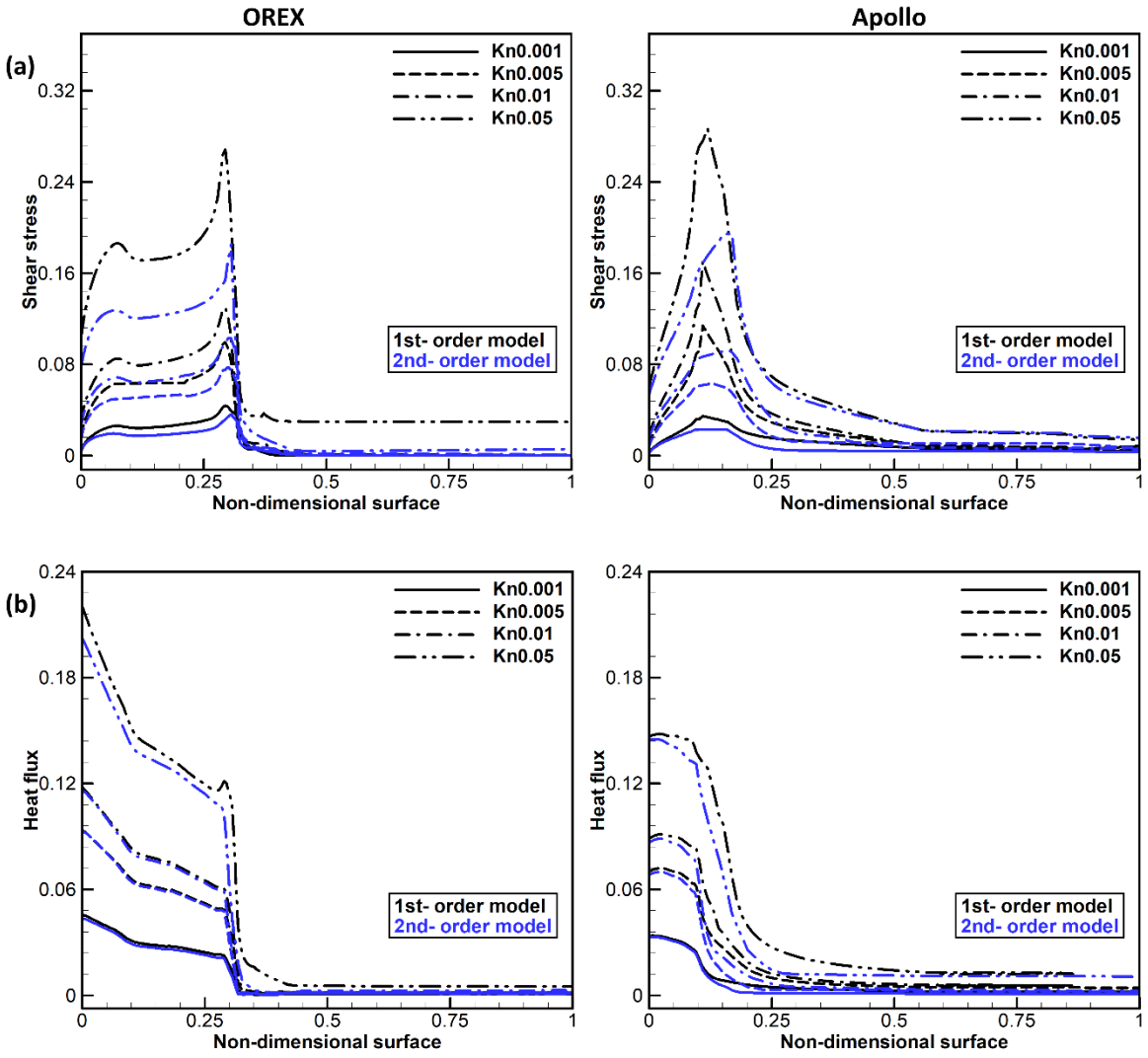

Fig. 10. Comparison of normalized surface variables for hypersonic rarefied nitrogen gas measured on the surfaces of the OREX (left side) and Apollo (right side) re-entry vehicles for varying degrees of rarefaction (N_δ) at $\alpha_A = 0^0$ and $M = 6$: (a) shear stress $\Pi_W / \left(\rho u_r^2 \right)$; (b) heat flux $Q_W / \left(\rho u_r^3 \right)$.

Next, we compared the normalized surface variables for hypersonic rarefied nitrogen gas over the OREX and Apollo vehicles for varying degrees of rarefaction, as illustrated in Fig. 10. It is seen that both normalized shear stress and heat flux over the re-entry vehicles increase with rarefaction, and the predicted surface heat flux over the OREX vehicle is comparatively higher. Moreover, compared with Fig. 8, both shear stress and heat flux values for the nitrogen gas are lower than that of argon gas. The decrease in shear stress can be related to the increase in intermolecular collisions which consequently decrease the momentum exchange with the surface. On the other hand, the increased heat flux for the argon gas can be associated with the larger values of temperature gradients near the surfaces of the re-entry vehicles. In general, the second-order model predicts lower shear stress and heat flux values than the first-order model.

Figure 11 compares the drag and heat flux coefficients for the hypersonic rarefied flow of nitrogen gas over the OREX and Apollo vehicles for varying degrees of rarefaction. As with argon gas, both the drag and heat flux coefficients increase with rarefaction because of the significant reduction in freestream values. Compared with Fig. 9, the aerothermodynamic force exerted by nitrogen gas over the re-entry vehicle is relatively lower than that of argon gas. Moreover, the increased bluntness of the Apollo vehicle experiences a relatively larger drag and lower heat flux. In general, the second-order model predicts these values further low.

Overall, the comparison of two-dimensional, geometric, and flow configurations of the re-entry vehicles suggests that the OREX vehicle experiences lower drag and higher aerothermodynamic heating than that of the Apollo vehicle under near/non-equilibrium flow regimes.

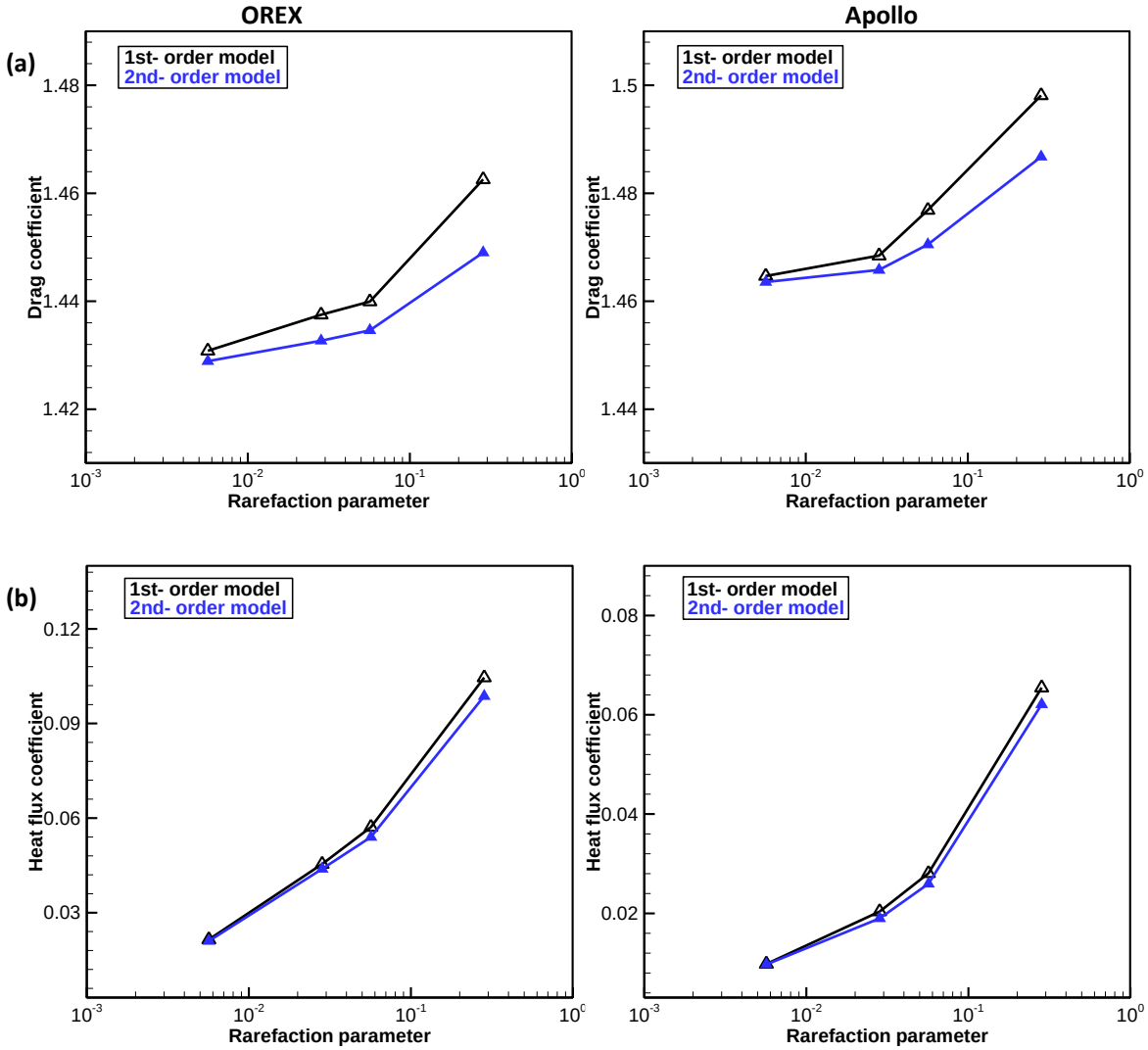

Fig. 11. Rarefaction effects on the aerothermodynamic data of hypersonic rarefied nitrogen gas flow over the OREX (left side) and Apollo (right side) re-entry vehicles for varying degrees of rarefaction (N_δ) at $\alpha_A = 0^0$ and $M = 6$: (a) drag coefficient; (b) heat flux.

4.3 Simulation of a 3D Apollo capsule: Effect of rotational degrees of freedom

A hypersonic (Mach number 6) flow of monatomic and diatomic gas was computed over a three-dimensional Apollo vehicle. The coefficient of the pitching moment about the z-direction was also considered (Priyadarshi P 2015; Moss, Glass, and Greene 2006; Singh 2018). The temperature of the freestream gas and the body surface was assumed to be a constant of 273 K. The computational domain consists of approximately 300,000 tetrahedral elements and 9,084 triangular elements for the surface. All numerical simulations were performed using the serial DG solver on an Intel Xeon workstation with a single processor, where no parallelization

scheme was incorporated. In the case of hypersonic gas flow ($M = 6$ and $\mathrm{Kn} = 0.05$) past a 3D Apollo vehicle, the computing time for the first-order and second-order constitutive models was found to be around 61 hours and 93 hours, respectively, resulting in a 52.4 % increase compared with the run time of the first-order model. The total forces and moments for nitrogen gas in each direction are calculated as (Singh 2018),

$$\begin{aligned} dF_x &= \left(-p - \left(\Pi_{xx} + \Delta\right)\right) n_x dydz + \left(-\Pi_{xy}\right) n_y dxdz + \left(-\Pi_{xz}\right) n_z dxdy, \\ dF_y &= \left(-\Pi_{xy}\right) n_x dydz + \left(-p - \left(\Pi_{yy} + \Delta\right)\right) n_y dxdz + \left(-\Pi_{yz}\right) n_z dxdy, \\ dF_z &= \left(-\Pi_{xz}\right) n_x dydz + \left(-\Pi_{yz}\right) n_y dxdz + \left(-p - \left(\Pi_{zz} + \Delta\right)\right) n_z dxdy. \end{aligned} \tag{51}$$

And the moments produced by these forces are represented as,

$$m = \int_{surface} \begin{bmatrix} yF_z - zF_y \\ zF_x - xF_z \\ xF_y - yF_x \end{bmatrix} dxdydz \,. \tag{52}$$

Figure 12 compares the pressure contours of the hypersonic rarefied flow of argon and nitrogen gases over a 3D Apollo vehicle obtained using the first- and second-order constitutive models for different freestream angles of attack $\left(\alpha_A\right)$ at Knudsen number 0.05. It is noted that a large amount of kinetic energy in the hypersonic freestream is converted by molecular collisions into the high thermal energy surrounding the reentry vehicle and by flow work into increased pressure. In this way, the region at the vicinity of the front surface is a zone of strong compression, with the maximum value obtained at $\alpha_A = 0^0$. Further, a comparison of monatomic and diatomic gases suggests that the stagnation pressure for argon gas is comparatively higher because of the reduced internal degrees of freedom. Similar findings were reported by Le et al. (Le et al. 2020) in their work, where the authors noticed a larger stagnation pressure for argon gas compared with the nitrogen gas for hypersonic flow over a cylinder using both OpenFOAM and DSMC simulations. Primarily, the shear-thinning characteristics of the second-order model allowed it to predict moderately lower values.

Argon

(a) $\alpha_A = 0^0$

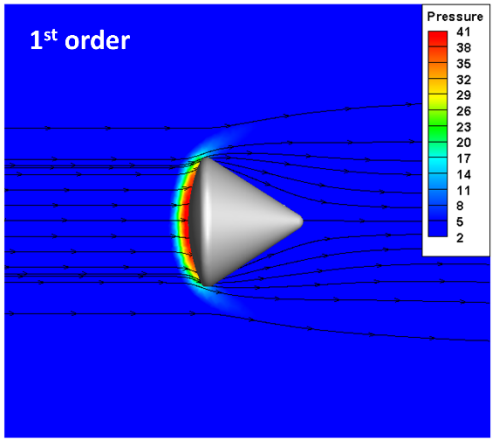

(b) $\alpha_A = 10^0$

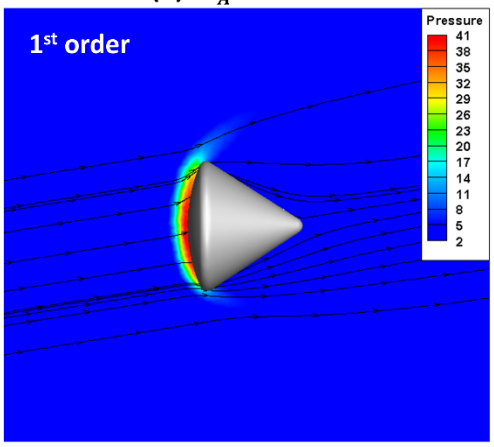

(a) $\alpha_A = 0^0$

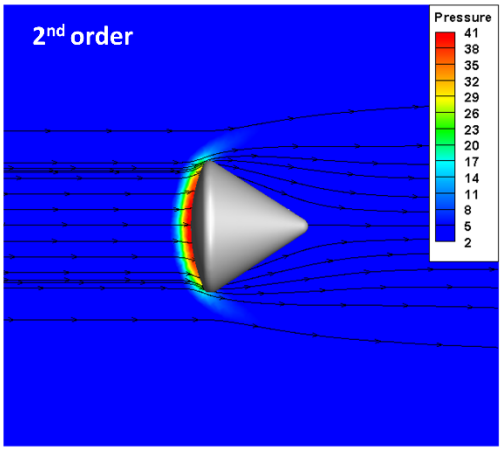

(b) $\alpha_A = 10^0$

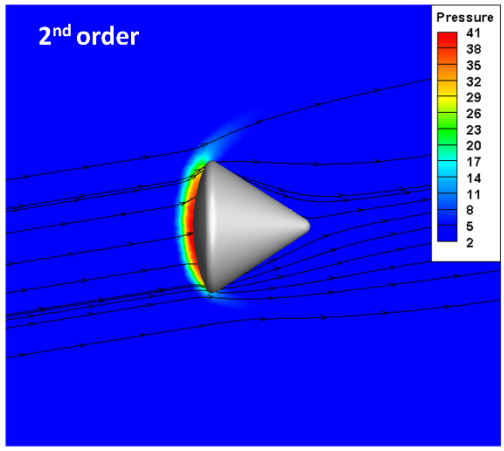

Nitrogen

(a) $\alpha_A = 0^0$

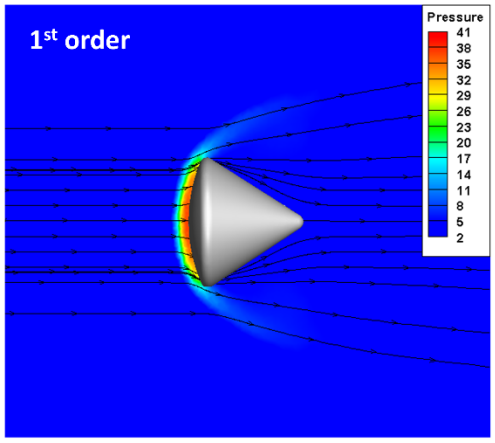

(b) $\alpha_A = 10^0$

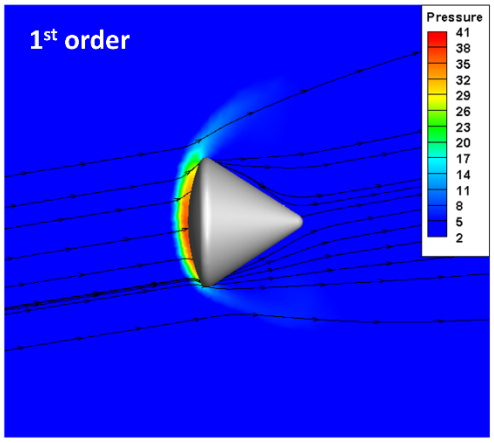

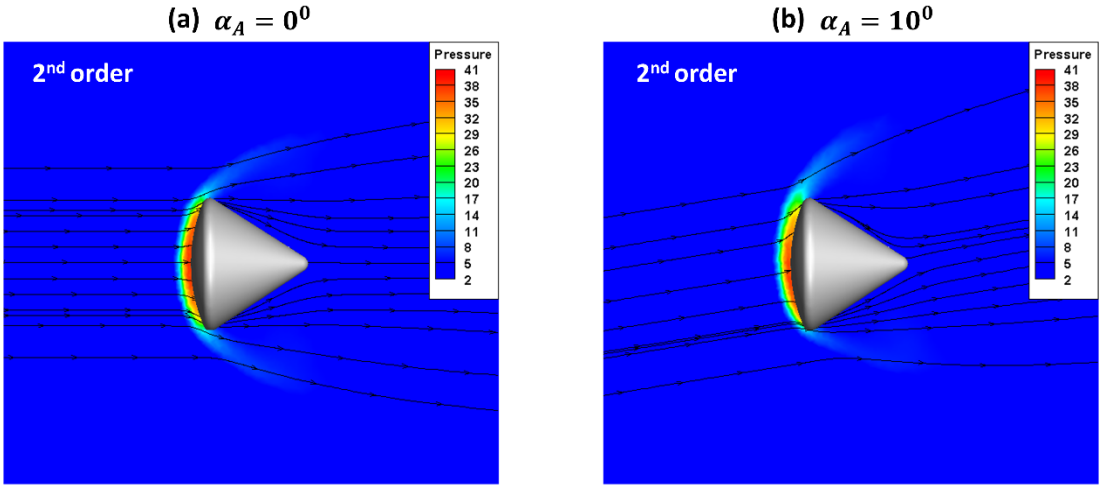

Fig. 12. Pressure contours of hypersonic rarefied argon (top) and nitrogen (bottom) gas flow over a three-dimensional Apollo vehicle obtained with the first- and second-order constitutive models for different freestream angles of attack at $M = 6$, $\mathrm{Kn} = 0.05$: (a) $\alpha_A = 0^0$; (b) $\alpha_A = 10^0$.

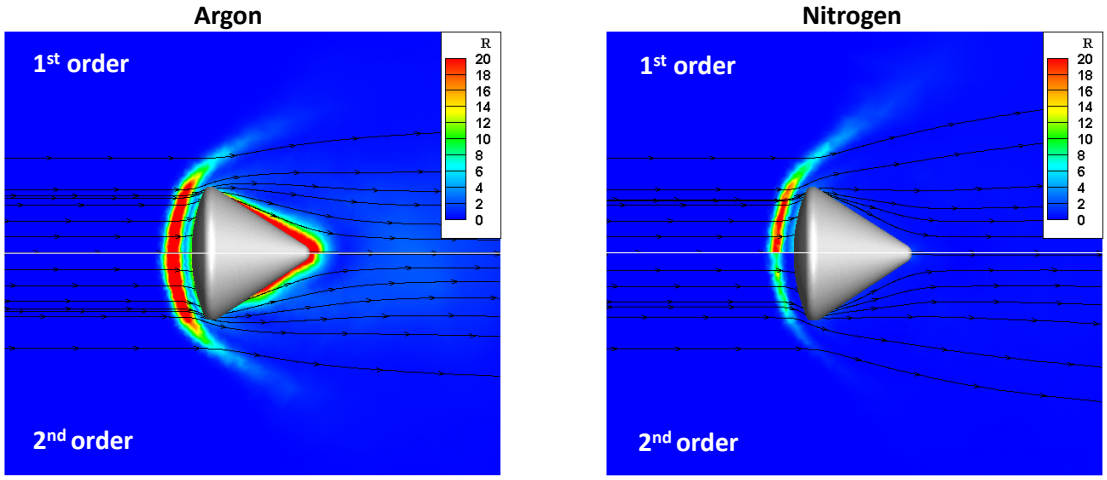

Fig. 13. Contours of the Rayleigh-Onsager dissipation function in a hypersonic rarefied flow of argon (left side) and nitrogen (right side) gases over a three-dimensional Apollo vehicle obtained with the first- and second-order constitutive models, at $\alpha_A = 0^0$, $M = 6$, and $\mathrm{Kn} = 0.05$.

Figure 13 shows a comparison of the contours of the Rayleigh-Onsager dissipation function obtained using the first- and second-order constitutive models for argon and nitrogen gases at zero degrees angle of attack and Knudsen number 0.05. The Rayleigh-Onsager dissipation $(\hat{R})$ plays a vital role in the theory of irreversible thermodynamics and is directly related to entropy production in non-equilibrium processes. The degree of local nonequilibrium is high in the bow shock region and the rear part of the Apollo vehicle where the flow experiences sudden changes. Moreover, it is noted that the degree of nonequilibrium is significantly higher for the argon gas than the nitrogen gas. The reason behind this physical phenomenon is the presence of significantly higher values of shear stress and heat flux in the bow shock region for the argon gas. Predominantly, it is observed that the first-order model over-predicts these values when compared with the second-order model, which is attributed to its limitation at high Knudsen and Mach number flows.

We also compared pressure contours for the hypersonic rarefied argon gas in Fig. 14 using the first-order constitutive model with and without slip and jump conditions to analyze the effect of slip and jump conditions. A significant increase in the stagnation pressure was noted for the first-order model without slip and jump conditions, leading to higher gradients in velocity and temperature near the re-entry vehicle. On the contrary, an increase in the gas-surface interactions was noted for the slip and jump conditions which in turn reduced the tangential velocity and temperature gradients near the surface, leading to lower stagnation pressure.

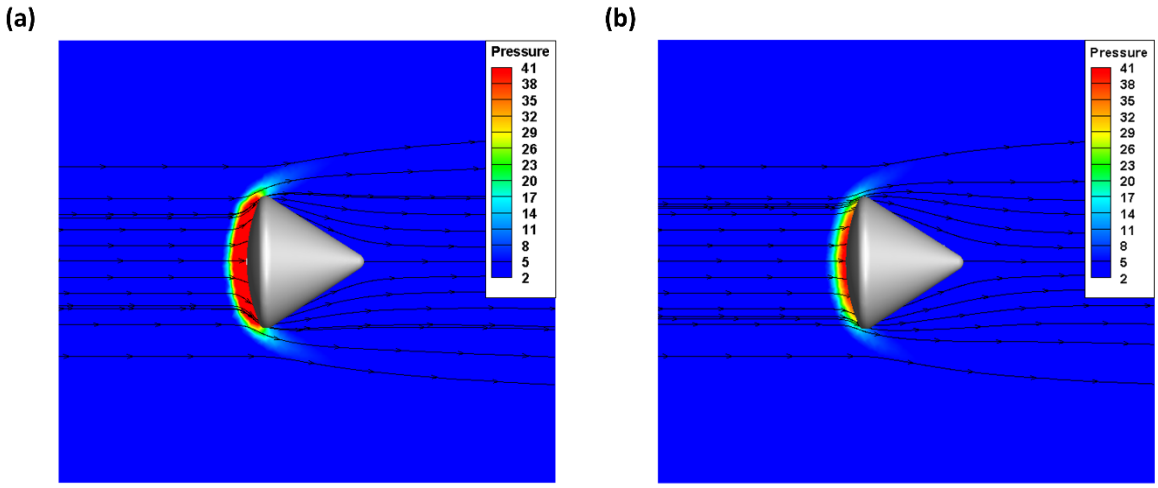

Fig. 14. Comparison of the pressure contours of hypersonic rarefied argon gas flow over a three-dimensional Apollo vehicle obtained using the first- constitutive models with or without slip/jump conditions at $\alpha_A = 0^0$, $M = 6$, $\mathrm{Kn} = 0.05$: (a) first-order model without slip and jump conditions; (b) first-order model with slip and jump conditions.

Figure 15 compares the lift-to-drag ratio, heat flux, and pitching moment coefficients for varying angles of attack and degree of rarefaction. As the degree of rarefaction and angles of attack increase, the lift-to-drag ratio is reduced considerably due to the change in the general flow pattern, which becomes smooth with an increased angle of attack. Furthermore, no major difference is noted between the values of lift-to-drag ratio for argon and nitrogen gases. On the other hand, a comparison of the heat flux coefficients suggests that the heat transfer is reduced with increasing angles of attack. The magnitude of the heat flux coefficient for argon gas is relatively higher than that of the nitrogen gas because of the higher stagnation temperature in the frontal part of the re-entry vehicle.

Further comparison of the pitching moment coefficient is presented in Fig. 1 (c). As the angles of attack and degree of rarefaction increase, the magnitude of the pitching moment coefficient (clockwise nose-up) along the z-direction increases, implying that the Apollo vehicle remains essentially unstable. However, compared with argon gas, the order of increase in the magnitude of the pitching moment coefficient is lower for nitrogen gas because of the reduced intermolecular interactions. In general, the first-order model over-estimates the

aerothermodynamic coefficients, leading to its poor performance under rarefied flow conditions. In addition, the comparison of with and without slip and jump conditions suggests that the first-order model without slip and jump (w/o slip) conditions predicts these coefficients substantially higher because of the increased gradients for the tangential velocity and temperature fields.

Finally, a comparison of the aerothermodynamic data with recent experimental work (Schlegat 2016) revealed that the qualitative trend in the plot of lift-to-drag ratio and pitching moment coefficients remained the same. A significant variation in the lift-to-drag ratio with increasing degree of rarefaction can be found because rarefaction has a stronger influence on the drag coefficient than the lift coefficient. When the drag coefficient was evaluated by integrating the surface pressure contribution from the projected frontal area, and the viscous contribution from the tangential forces at the wall, its effect became significant with rarefaction. Lift, on the other hand, has dominant pressure and negligible viscous part at low angles of attack. At higher angles of attack, the viscous part on the lift becomes noticeable; however, its effect is not as strong as its counterpart. The reduced lift-to-drag ratio can cause the re-entry vehicle to dive deeper into the atmosphere.

Conversely, the pitching moment is very sensitive to the location where the resultant dynamic pressure force attacks. That means if an aerodynamic force pushes the vehicle away from its original trimmed flight condition, a counteracting pitching moment is generated to move the vehicle back to its original flight altitude, whereby an aerodynamic static stability is attained. In the present scenario, as the rarefaction is increased, a continual increase in the order of pitching moment is noticed. This indicates that the body flap of the reentry vehicle is too short for the position of the center of gravity, leading to a statically unstable flight transition, in agreement with the measured aerodynamic data illustrated in Fig. 4 (Schlegat 2016). The effect of rarefaction was observed to be stronger at higher angles of attack, as the pitching moment coefficient varied considerably, resulting in a statically unstable transition during re-entry.

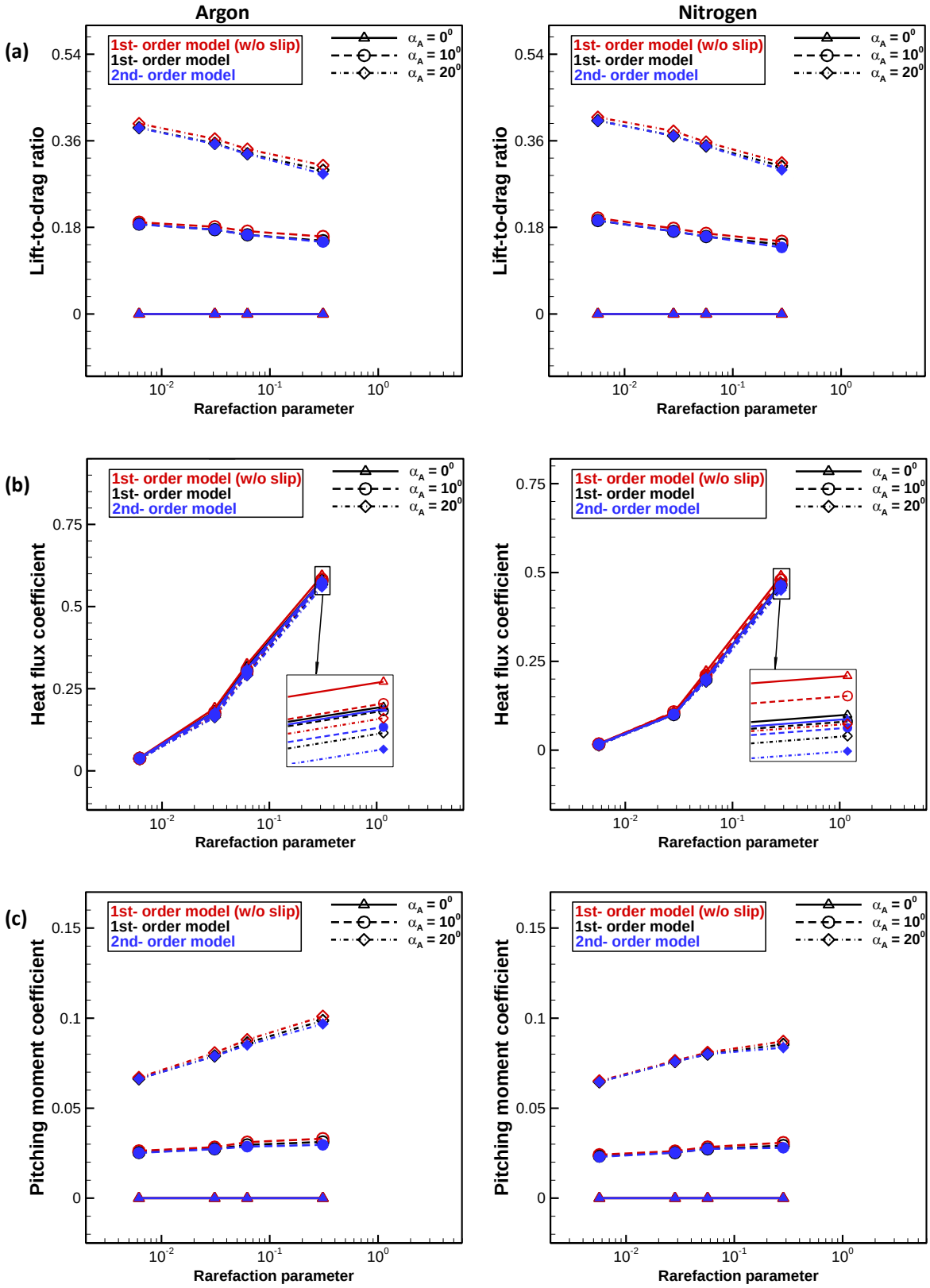

Fig. 15. Bulk viscosity effects on aerothermodynamic data obtained using the first- and second-

order constitutive models for the hypersonic rarefied flow of argon (left side) and nitrogen (right side) gases over a three-dimensional Apollo vehicle for varying degrees of rarefaction (N_δ) and different freestream angles of attack at $M = 6$: (a) lift-to-drag ratio; (b) heat flux coefficient; (c) pitching moment coefficient.

5. Summary and conclusions

We investigated the non-equilibrium effects of monatomic and diatomic gases experienced by hypersonic re-entry vehicles using the mixed modal discontinuous Galerkin (DG) formulations. In the mixed modal DG scheme, auxiliary variables were introduced to solve the nonlinear second-order constitutive relations of non-conserved variables which describe monatomic and diatomic gases in strong thermal nonequilibrium. Additionally, velocity slip and temperature jump boundary conditions were implemented at the surfaces for the multi-dimensional DG code. To ascertain numerical accuracy, hierarchical basis functions based on the orthogonal Jacobi polynomials for triangular and tetrahedral elements were incorporated. For temporal discretization, a third-order accurate SSP-RK scheme that preserves the monotonicity of the spatial discretization was employed.

The results showed that the rotational mode of energy transfer plays a crucial role in nitrogen gas away from equilibrium. Notable differences were seen in the flow fields and measured surface quantities for monatomic and diatomic gas over different configurations of re-entry vehicles. Distinctively, weaker shock waves and reduced overall stagnation temperature in the frontal region of the re-entry vehicle were noted for nitrogen gas compared with argon gas. Consequently, reduced aerothermodynamic forces were exerted by nitrogen gas on the re-entry vehicle. Further, a detailed comparison of different configurations of re-entry vehicles suggests that the OREX vehicle experienced a relatively lower drag and enhanced heat flux than the Apollo vehicle under near/non-equilibrium regimes.

With increasing rarefaction and flow angles of attack, a considerable loss in the lift-to-drag ratio was noticed, in contrast to the heat flux coefficients. Also, the magnitude of the nose-up pitching moment coefficient was notably enhanced by the angles of attack and rarefaction, implying that the re-entry vehicle was susceptible to a loss of stability. The order of increase

in the magnitude of the pitching moment was relatively higher for argon gas than nitrogen gas because of the reduced internal degrees of freedom. Altogether, the analysis of the first- and second-order constitutive models indicated that the first-order model over-predicted the results when compared with the second-order model at higher degrees of non-equilibrium.

The shortcoming of the first-order model was overcome by the inclusion of the second-order model. However, at hypersonic Mach numbers sufficiently above 6 and low altitudes, the flow becomes more complicated for the nitrogen gas molecules, with increased internal energies and chemical reactions. In addition, ionization, thermal radiation, and electronic excitation usually intensify under these non-equilibrium flow regimes. In the future, we hope to report DG-based computational models which include vibrational and chemical non-equilibrium effects.

Acknowledgments

This work was supported by the National Research Foundation of Korea funded by the Ministry of Science and ICT (NRF 2017-R1A2B2007634 and NRF 2017-R1A5A1015311), South Korea.

References

Alekseenko, A., N. Gimelshein, and S. Gimelshein. 2012. “An application of discontinuous Galerkin space and velocity discretisations to the solution of a model kinetic equation.” *International Journal of Computational Fluid Dynamics* 26(3):145-161.

Barter, G.E., and D.L. Darmofal. 2010. “Shock capturing with PDE-based artificial viscosity for DGFEM: Part I. Formulation.” *Journal of Computational Physics* 229(5):1810-27.

Bassi, F., and S. Rebay. 1997. “A high-order accurate discontinuous finite element method for the numerical solution of the compressible Navier–Stokes equations.” *Journal of Computational Physics* 131(2):267-79.

Belouaggadia, N., H. Olivier, and R. Brun. 2008. “Numerical and theoretical study of the shock stand-off distance in non-equilibrium flows,” *Journal of Fluid Mechanics* 607:167-197.

Bird, G.A. 1994. *Molecular Gas Dynamics and the Direct Simulation of Gas Flows*. Vol. 5: Clarendon Press, Oxford.

Bochev, P.B., and J. Choi. 2001. “A comparative study of least-squares, SUPG and Galerkin methods for convection problems.” *International Journal of Computational Fluid Dynamics* 15(2):127-146.

Brazell, M.J., and D.J. Mavriplis. 2013. “3D mixed element discontinuous Galerkin with shock capturing.” *AIAA Paper 2013-3064*, The 21st AIAA Computational Fluid Dynamics Conference.

Burgess, N., and D. Mavriplis. 2012. “Computing shocked flows with high-order accurate discontinuous Galerkin methods.” *AIAA Paper 2012-2715*, 42nd AIAA Fluid Dynamics Conference and Exhibit.

Chae, J.H., T.K. Mankodi, S.M. Choi, and R.S. Myong. 2020. “Combined effects of thermal non-equilibrium and chemical reactions on hypersonic air flows around an orbital reentry vehicle.”

International Journal of Aeronautical and Space Science 21:612-626.
Chapman, S., and T.G. Cowling. 1990. *The Mathematical Theory of Non-uniform Gases: an Account of the Kinetic Theory of Viscosity, Thermal Conduction and Diffusion in Gases*: Cambridge University Press.
Ching, E.J., Y. Lv, P. Gnoffo, M. Barnhardt, and M. Ihme. 2019. "Shock capturing for discontinuous Galerkin methods with application to predicting heat transfer in hypersonic flows." *Journal of Computational Physics* 376:54-75.
Chinnappan, A.K., G. Malaikannan, and R. Kumar. 2017. "Insights into flow and heat transfer aspects of hypersonic rarefied flow over a blunt body with aerospike using direct simulation Monte-Carlo approach." *Aerospace Science and Technology* 66:119-28.
Chourushi, T., A. Rahimi, S. Singh, O. Ejethadi, T.K. Mankodi, and R.S. Myong. 2022. "Thermal and flow characteristics of nonequilibrium monatomic, diatomic, and polyatomic gases in cylindrical Couette flow based on second-order non-Navier–Fourier constitutive model." *In Press*, *International Journal of Heat and Mass Transfer*. https://doi.org/10.1016/j.ijheatmasstransfer.2022.122580
Chourushi, T., A. Rahimi, S. Singh, and R.S. Myong. 2020. "Computational simulations of near-continuum gas flow using Navier-Stokes-Fourier equations with slip and jump conditions based on the modal discontinuous Galerkin method." *Advances in Aerodynamics* 2:1-37.
Chourushi, T., S. Singh, and R.S. Myong. 2018. "Computational study of rarefied flow inside a lid driven cavity using a mixed modal discontinuous galerkin method." *Journal of Computational Fluids Engineering* 23(3):62-71.
Cockburn, B., and C.W. Shu. 1998. "The Runge–Kutta discontinuous Galerkin method for conservation laws V: multidimensional systems." *Journal of Computational Physics* 141 (2):199-224.
Cramer, M.S. 2012. "Numerical estimates for the bulk viscosity of ideal gases." *Physics of Fluids* 24 (6):066102.
Curtiss, C.F. 1981. "The classical Boltzmann equation of a gas of diatomic molecules." *The Journal of Chemical Physics* 75 (1):376-8.
de Góes Maciel, E.S. 2015. "Magnetic field applied to thermochemical non-equilibrium reentry flows in 2D–five species." *International Journal of Computational Fluid Dynamics* 29 (6-8):376-99.
Dellacherie, S. 2010. "Analysis of Godunov type schemes applied to the compressible Euler system at low Mach number." *Journal of Computational Physics* 229:978-1016.
Dubiner, M. 1991. "Spectral methods on triangles and other domains." *Journal of Scientific Computing* 6(4):345-90.
Ejtehadi, O., A. Rahimi, A. Karchani, and R.S. Myong. 2018. "Complex wave patterns in dilute gas–particle flows based on a novel discontinuous Galerkin scheme." *International Journal of Multiphase Flow* 104:125-51.
Ejtehadi, O., A. Rahimi, and R.S. Myong. 2020. "Investigation of a trifold interaction mechanism of shock, vortex, and dust using a DG method in a two-fluid model framework." *Powder Technology* 374:121-38.
Ejtehadi, O., and R.S. Myong. 2020. "A modal discontinuous Galerkin method for simulating dusty and granular gas flows in thermal non-equilibrium in the Eulerian framework." *Journal of Computational Physics* 411:109410.
Eu, B.C. 1980. "A modified moment method and irreversible thermodynamics." *The Journal of Chemical Physics* 73(6):2958-69.
Eu, B.C. 1981. "Nonlinear transport processes in gases." *The Journal of Chemical Physics* 74(5):3006-15.
Eu, B.C. 1992. *Kinetic Theory and Irreversible Thermodynamics*. In.: Wiley-Interscience.
Eu, B.C., and Y.G. Ohr. 2001. "Generalized hydrodynamics, bulk viscosity, and sound wave absorption and dispersion in dilute rigid molecular gases." *Physics of Fluids* 13 (3):744-53.
Evans, B., K. Morgan, and O. Hassan. 2011. "A discontinuous finite element solution of the Boltzmann kinetic equation in collisionless and BGK forms for macroscopic gas flows." *Applied*

Mathematical Modelling 35(3):996-1015.
Evans, B., M. Hanna, M. Dawson, and M. Mesiti. 2019. "High order parallelisation of an unstructured grid, discontinuous-Galerkin finite element solver for the Boltzmann–BGK equation." *International Journal of Computational Fluid Dynamics* 33(8):343-351.
Franchina, N., S. Fernández-Méndez, and R. Sevilla. 2019. "Discontinuous Galerkin methods–new trends and applications." *International Journal of Computational Fluid Dynamics* 33(8):333-334.
Giraldo, F.X., and T. Warburton. 2008. "A high-order triangular discontinuous Galerkin oceanic shallow water model." *International Journal for Numerical Methods in Fluids* 56 (7):899-925.
Grad, H. 1949. "On the kinetic theory of rarefied gases." *Communications on Pure and Applied Mathematics* 2(4):331-407.
Guo, J., G. Lin, J. Zhang, X. Bu, and H. Li. 2019. "Hypersonic aerodynamics of a deformed aeroshell in continuum and near-continuum regimes." *Aerospace Science and Technology* 93:105296.
Hash, D., J. Olejniczak, M. Wright, D. Prabhu, M. Pulsonetti, B. Hollis, P. Gnoffo, M. Barnhardt, I. Nompelis, and G. Candler. 2007. "FIRE II calculations for hypersonic nonequilibrium aerothermodynamics code verification: DPLR, LAURA, and US3D." *AIAA Paper 2007-605*, The 45th AIAA Aerospace Sciences Meeting and Exhibit.
Hollis, B.R., and S. Borrelli. 2012. "Aerothermodynamics of blunt body entry vehicles." *Progress in Aerospace Sciences* 48:42-56.
Hwang, P.F.. 1971. *A Kinetic Theory Description of Rarefied Gas Flows with the Effect of Rotational Relaxation*. PhD Thesis, Georgia Institute of Technology.
Iannelli, J. 2011. "An implicit Galerkin finite element Runge–Kutta algorithm for shock-structure investigations." *Journal of Computational Physics* 230(1):260-86.
Jiang, D., M. Mao, J. Li, and X. Deng. 2019. "An implicit parallel UGKS solver for flows covering various regimes." *Advances in Aerodynamics* 1(1):8.
Jiang, Z., W. Zhao, Z. Yuan, W. Chen, and R.S. Myong. 2019. "Computation of hypersonic flows over flying configurations using a nonlinear constitutive model." *AIAA Journal* 57:5252-68.
Jiang, Z., W. Zhao, W. Chen, and R.K. Agarwal. 2019. "Computation of shock wave structure using a simpler set of generalized hydrodynamic equations based on nonlinear coupled constitutive relations." *Shock Waves* 29(8):1227-39.
Jiang, Z., W. Zhao, W. Chen, and R.K. Agarwal. 2019. "An undecomposed hybrid algorithm for nonlinear coupled constitutive relations of rarefied gas dynamics." *Communications in Computational Physics* 26(3):880-912.
Karchani, A., and R.S. Myong. 2016. "Performance of limiters in modal discontinuous Galerkin methods for 1-D Euler equations." *Journal of Computational Fluids Engineering* 21(2):1-11.
Kennard, E.H. 1938. *Kinetic Theory of Gases, with an Introduction to Statistical Mechanics*. London: McGraw-Hill.
Le, N.T.P., H. Xiao, and R.S. Myong. 2014. "A triangular discontinuous Galerkin method for non-Newtonian implicit constitutive models of rarefied and microscale gases." *Journal of Computational Physics* 273:160-84.
Le, N.T.P., N.H. Tran, T.N. Tran, and T.T. Tran. 2020. "New slip boundary condition in high-speed rarefied gas flow simulations." *Proceedings of the Institution of Mechanical Engineers, Part G: Journal of Aerospace Engineering,* 234(3):840-856.
Li, B.Q. 2006. *Discontinuous Finite Elements in Fluid Dynamics and Heat Transfer*: Springer Science & Business Media.
Li, L., and Q. Zhang. 2017. "A new vertex-based limiting approach for nodal discontinuous Galerkin methods on arbitrary unstructured meshes." *Computers & Fluids* 159:316-26.
Li, Z.H., and H.X. Zhang. 2009. "Gas-kinetic numerical studies of three-dimensional complex flows on spacecraft re-entry." *Journal of Computational Physics* 228(4):1116-38.
Liang, J., Z.H. Li, X.G. Li, and W.B. Shi. 2018. "Monte Carlo simulation of spacecraft reentry aerothermodynamics and analysis for ablating disintegration." *Communications in*

Computational Physics 23(4):1037-51.
Lofthouse, A.J., L.C. Scalabrin, and I.D. Boyd. 2008. "Velocity slip and temperature jump in hypersonic aerothermodynamics." *Journal of Thermophysics and Heat Transfer* 22(1):38-49.
Mankodi, T.K., U.V. Bhandarkar, and R.S. Myong. 2020. "Collision cross sections and nonequilibrium viscosity coefficients of N2 and O2 based on molecular dynamics." *Physics of Fluids* 32(3):036102.
McCourt, F.R.W., J.J.M. Beenakker, W.E. Köhler, and I. Kuščer. 1990. *Nonequilibrium Phenomena in Polyatomic Gases: Volume 1 Dilute Gases*: Clarendon Press, Oxford.
Moss, J., C. Glass, and F. Greene. 2006. "DSMC simulations of Apollo capsule aerodynamics for hypersonic rarefied conditions." *AIAA Paper 2006-3577*, The 9th AIAA/ASME Joint Thermophysics and Heat Transfer Conference.
Myong, R.S. 1999. "Thermodynamically consistent hydrodynamic computational models for high-Knudsen-number gas flows." *Physics of Fluids* 11(9):2788-802.
Myong, R.S. 2001. "A computational method for Eu's generalized hydrodynamic equations of rarefied and microscale gasdynamics." *Journal of Computational Physics* 168(1):47-72.
Myong, R.S. 2004a. "Gaseous slip models based on the Langmuir adsorption isotherm." *Physics of Fluids* 16(1):104-17.
Myong, R.S. 2004b. "A generalized hydrodynamic computational model for rarefied and microscale diatomic gas flows." *Journal of Computational Physics* 195(2):655-76.
Myong, R.S. 2011. "A full analytical solution for the force-driven compressible Poiseuille gas flow based on a nonlinear coupled constitutive relation." *Physics of Fluids* 23(1):012002.
Myong, R.S. 2014. "On the high Mach number shock structure singularity caused by overreach of Maxwellian molecules." *Physics of Fluids* 26 (5):056102.
Myong, R.S. 2016. "Theoretical description of the gaseous Knudsen layer in Couette flow based on the second-order constitutive and slip-jump models." *Physics of Fluids* 28(1):012002.
Myong, R.S., J.M. Reese, R.W. Barber, and D.R. Emerson. 2005. "Velocity slip in microscale cylindrical Couette flow: the Langmuir model." *Physics of Fluids* 17(8):087105.
Noori, S., and S.M.H. Karimian. 2008. "Using axisymmetric analogue along the streamlines for the solution of three-dimensional viscous shock layer equations of hypersonic equilibrium flow." *International Journal of Computational Fluid Dynamics* 22(6):429-36.
Onsager, L. 1931. "Reciprocal relations in irreversible processes. II." *Physical Review* 38:2265-79.
Peng, A.P., Z.H. Li, J.L. Wu, and X.Y. Jiang. 2016. "Implicit gas-kinetic unified algorithm based on multi-block docking grid for multi-body reentry flows covering all flow regimes." *Journal of Computational Physics* 327:919-42.
Priyadarshi, P. 2015. *Multifidelity Multiobjective Multidisciplinary Design Optimization (M3DO) of a Semi-ballistic Reentry Vehicle*. PhD Thesis, Indian Institute of Technology Kanpur.
Raj, L.P., S. Singh, A. Karchani, and R.S. Myong. 2017. "A super-parallel mixed explicit discontinuous Galerkin method for the second-order Boltzmann-based constitutive models of rarefied and microscale gases." *Computers & Fluids* 157:146-63.
Santos, W.F. 2007. "Simulation of blunt leading edge aerothermodynamics in rarefied hypersonic flow." *Journal of the Brazilian Society of Mechanical Sciences and Engineering* 29(2):123-35.
Sawley, M.L., and S. Wüthrich. 1995. "On the influence of the choice of transport and chemical models for non-equilibrium hypersonic flow simulations." *International Journal of Computational Fluid Dynamics* 4(1-2):87-110.
Schlegat, T. 2016. *Experimental Investigation of Rarefaction Effects on Aerodynamic Coefficients of Slender and Blunt Re-entry Vehicles*. PhD Thesis, DLR Deutsches Zentrum für Luft- und Raumfahrt e.V. - Forschungsberichte 23:1-134.
Schouler, M., Y. Prévereaud, and L. Mieussens. 2020. "Survey of flight and numerical data of hypersonic rarefied flows encountered in earth orbit and atmospheric reentry." *Progress in Aerospace Sciences* 118:100638.
Schwartzentruber, T., and I. Boyd. 2008. "Investigation of continuum breakdown in hypersonic flows

using a hybrid DSMC-NS algorithm." *AIAA Paper 2008-4108*.
Schwartzentruber, T., and I. Boyd. 2015. "Progress and future prospects for particle-based simulation of hypersonic flow." *Progress in Aerospace Sciences* 72:66-79.
Shu, C.W. 2016. "Discontinuous Galerkin methods for time-dependent convection dominated problems: Basics, recent developments and comparison with other methods." *In Building Bridges: Connections and Challenges in Modern Approaches to Numerical Partial Differential Equations*, 371-399, Springer.
Singh, S., and R.S. Myong. 2017. "A computational study of bulk viscosity effects on shock-vortex interaction using discontinuous Galerkin method." *Journal of Computational Fluids Engineering* 22(2):86-95.
Singh, S., A. Karchani, and R.S. Myong. 2018. "Non-equilibrium effects of diatomic and polyatomic gases on the shock-vortex interaction based on the second-order constitutive model of the Boltzmann-Curtiss equation." *Physics of Fluids* 30(1):016109.
Singh, S. 2018. *Development of a 3D Discontinuous Galerkin Method for the Second-order Boltzmann-Curtiss Based Hydrodynamic Models of Diatomic and Polyatomic Gases*. PhD Thesis, Gyeongsang National University.
Singh, S., and R.S. Myong. 2019. "Three-dimensional discontinuous Galerkin method for the second-order Boltzmann-Curtiss constitutive model in continuum-rarefied gas flows." *AIP Conference Proceedings 2132,* 060013.
Singh, S., and M. Battiato. 2020. "Strongly out-of-equilibrium simulations for electron Boltzmann transport equation using modal discontinuous Galerkin approach." *International Journal of Applied and Computational Mathematics* 6(5):133.
Singh, S., A. Karchani, K. Sharma, and R.S. Myong. 2020. "Topology of the second-order constitutive model based on the Boltzmann–Curtiss kinetic equation for diatomic and polyatomic gases." *Physics of Fluids* 32(2):026104.
Singh, S., and M. Battiato. 2021a. "Behavior of a shock-accelerated heavy cylindrical bubble under nonequilibrium conditions of diatomic and polyatomic gases." *Physical Review Fluids* 6(4):044001.
Singh, S., and M. Battiato. 2021b. "An explicit modal discontinuous Galerkin method for Boltzmann transport equation under electronic nonequilibrium conditions." *Computers & Fluids* 224:104972.
Singh, S., M. Battiato, and R.S. Myong. 2021. "Impact of bulk viscosity on flow morphology of shock-accelerated cylindrical light bubble in diatomic and polyatomic gases." *Physics of Fluids* 33(6):066103.
Singh, S., A. Karchani, T. Chourushi, and R.S. Myong. 2022. "A three-dimensional modal discontinuous Galerkin method for the second-order Boltzmann-Curtiss-based constitutive model of rarefied and microscale gas flows." *In Revision*.
Smoluchowski, V.S.M. 1898. "Ueber wärmeleitung in verdünnten gasen." *Annalen der Physik* 300(1):101-30.
Su, W., P. Wang, and Y. Zhang. 2019. "High-order hybridisable discontinuous Galerkin method for the gas kinetic equation." *International Journal of Computational Fluid Dynamics* 33(8):335-342.
Tsai, C.Y., R. Chue, C. Nicholson, and J. Tyll. 2009. "Hypervelocity capability of HyPulse Shock Tunnel for radiative heat transfer measurements at lunar reentries." *AIAA Paper 2009-1516*.
Tsien, H.S. 1946. "Superaerodynamics, mechanics of rarefied gases." *Journal of the Aeronautical Sciences* 13(12):653-64.
Xiao, H., and R.S. Myong. 2014. "Computational simulations of microscale shock–vortex interaction using a mixed discontinuous galerkin method." *Computers & Fluids* 105:179-93.
Yoshinaga, T., A. Tate, M. Watanabe, and T. Shimoda. 1996. "Orbital re-entry experiment vehicle ground and flight dynamic test results comparison." *Journal of Spacecraft and Rockets* 33(5):635-42.
You, H., and C. Kim. 2019. "Direct reconstruction method for discontinuous Galerkin methods on

higher-order mixed-curved meshes I. Volume integration." *Journal of Computational Physics* 395:223-46.
Yuan, Z., W. Zhao, Z. Jiang, and W. Chen. 2021. "Numerical simulation of hypersonic reaction flows with nonlinear coupled constitutive relations." *Aerospace Science and Technology* 112:106591.
Zhang, W.M., G. Meng, and X. Wei. 2012. "A review on slip models for gas microflows." *Microfluidics and Nanofluidics* 13(6):845-82.